



# Effect of elastocapillarity on the swelling kinetics of hydrogels

Ida Ang<sup>a</sup>, Zezhou Liu<sup>a,b</sup>, Jaemin Kim<sup>a,b</sup>, Chung-Yuen Hui<sup>a,b,c</sup>,  
Nikolaos Bouklas<sup>a,b,\*</sup>

<sup>a</sup> Sibley School of Mechanical and Aerospace Engineering, Cornell University, Ithaca, NY 14853, USA

<sup>b</sup> Field of Theoretical and Applied Mechanics, Cornell University, Ithaca, NY 14853, USA

<sup>c</sup> Global Station for Soft Matter, GI-CoRE, Hokkaido University, Sapporo, Japan



## ARTICLE INFO

### Article history:

Received 25 June 2020

Revised 31 July 2020

Accepted 25 August 2020

Available online 27 August 2020

### Keywords:

Hydrogels

Elastocapillarity

Surface stress

Swelling

Surface energy

## ABSTRACT

The swelling behavior of hydrogels, involving coupled diffusion and large deformations, makes them ideal for biomedical applications such as micro- and nano-scale drug delivery systems. Understanding the transient swelling or drying behavior of hydrogels at relevant length-scales will provide insight for the development of specialized and controlled drug release. At sub-millimeter length-scales, surface stresses have been shown to significantly influence material behavior for soft polymers and hydrogels, but very little is known about the influence of surface stresses on the swelling kinetics of hydrogels. In this paper, we present a non-linear theory and mixed finite element formulation that takes into account mass transport, large deformations, and elastocapillary effects for hydrogels. Focusing on hydrogel micro-spheres, we provide a comparison of swelling kinetics between the presented non-linear theory and an analytical solution using linear poroelasticity that incorporates surface stresses. Our results demonstrate that when the surface free energy is constant per unit current area (fluid-like) and the elastocapillary length-scale is on the order of the size of the hydrogel micro-sphere, the transient response equilibrates approximately an order of magnitude faster in time compared to the case without surface effects irrespective of swelling or drying. This difference in equilibration time suggests the interplay between competing processes of solvent diffusion, large deformations, and surface effects. Furthermore, we demonstrate that a Neo-Hookean type surface free energy can result in an even faster equilibration as compared to a fluid-like surface free energy. Lastly, our finite element implementation predicts the transient response of complex shapes and constrained structures.

© 2020 Elsevier Ltd. All rights reserved.

## 1. Introduction

A hydrogel consists of solvent and polymer chains cross-linked to form a 3D elastomeric network. Solvent can diffuse in the elastomeric network, leading to large and reversible swelling/drying deformations. The complex response of hydrogels can be controlled with changes in environmental stimuli including temperature, pH, and electric fields (Ahn et al., 2008; Liu et al., 2015). Hydrogels are used in a wide variety of technologies: flexible electronics, soft robotics, medical imaging, wound healing, tissue scaffolding, and drug delivery methods (Choi et al., 2007; Li and Suo, 2006; Peppas et al., 2006;

\* Corresponding author at: Cornell University, Ithaca, NY 14853, United States.

E-mail address: [nb589@cornell.edu](mailto:nb589@cornell.edu) (N. Bouklas).

Polygerinos et al., 2017). In the biomedical field, many of the aforementioned applications have been investigated because of the ability to tune physical and biological aspects of the hydrogel fabrication procedure (Elkhoury et al., 2019). In drug delivery, materials can be chosen with regards to biocompatibility to suppress the immune response (Hennink and van Nostrum, 2002). Furthermore, soft solids exhibit low stiffness which helps prevent surrounding tissue irritation if the hydrogel swells significantly (Bhattarai et al., 2010; Hennink and van Nostrum, 2002).

The challenge in drug delivery is bioavailability, the amount of drug present in the circulatory system for a therapeutic effect after administration. Drug agents that demonstrated therapeutic effects in clinical trials were unable to be utilized commercially because of low bioavailability (Steichen et al., 2013). To increase the efficacy of these types of drugs, different delivery methods have been studied. These methods include fabricating hydrogel micro or nanoparticles with a therapeutic agent in order to control drug release, as seen in Peppas et al. (2006), or utilizing capillary-induced instabilities for self-folding polymers, as seen in Fernandes and Gracias (2012). We consider cases of encapsulation or conjugation of the hydrogel with the drug, where the drug is released in a controlled time-dependent manner as the hydrogel swells. The process of encapsulation of the drug within the nanoparticle could increase bioavailability by allowing the drug to travel to the target site, protected from degradation by the hydrogel.

Prior experimental and computational studies have demonstrated that nanoparticle properties such as geometry (size and shape), surface charge, and material composition, affect uptake by cells (Agarwal et al., 2013; Calderera-Moore et al., 2011; Zhang et al., 2012). Work by Agarwal et al. (2013) demonstrates that nano-disks with high aspect ratios demonstrate higher uptake rates than nano-rods in mammalian cells. Zhang et al. (2012) provides a comparison of nano-disks to nano-spheres and shows that nano-disks are preferred for cell surface binding based on their larger contact surface, while nano-spheres are preferred for cellular uptake. These findings provide the motivation for studying micro-sphere swelling. Nevertheless, while swelling is of interest for drug release, it is a reversible process, and drying can occur depending on the surrounding environment. Experimentally, it has been observed that swelling and drying display asymmetric time-dependent kinetics (Bertrand et al., 2016; Chen et al., 2020). In other words, drying is not simply a reversal of swelling in terms of time-dependent behavior, and must be analyzed independently (Chen et al., 2020).

Understanding how elastocapillary phenomena affect hydrogel behavior can improve the ways hydrogels are utilized in technology today. It is well known that surface energy has an effect on the behavior of liquids, but typically has a negligible effect in solids in the macroscale (Style et al., 2017). However, soft elastomers and hydrogels are known to exhibit elastocapillary effects at length-scales up to the order of millimeters (Bico et al., 2018). Surface effects are also critical in soft-tissue morphogenetic processes such as embryogenesis and wound healing, which involves feature formation and growth (Maidland et al., 2019). Surface effects are prominent when the surface energy contribution is comparable to the bulk energetic contributions. The elastocapillary length-scale dictates when surface effects are a significant driving force of material response.

In general, surface stresses minimize the surface area and round-off sharp features of solid surfaces (Hui et al., 2002; Lapinski et al., 2019; Mora et al., 2013). Classically, surface stress in hydrogels is treated as a constant isotropic tensor (equivalent with surface tension which is a scalar), but recent experiments have demonstrate that surface stress is strain dependent (Jensen et al., 2017; Style and Xu, 2018; Xu et al., 2018). This finding has implications for adhesionless and adhesive contact, where classical theories such as the Hertz theory or Johnson-Kendall-Robert theory have to be reformulated (Hui et al., 2015; Liu et al., 2020c). Hydrogel (Kang and Huang, 2010) and elastomer bi-layers (Alawiye et al., 2019) have been shown to exhibit swell-induced instabilities that can be suppressed or delayed through the effect of surface stresses. Therefore, during the fabrication and release of hydrogel nano-particles, elastocapillarity must be taken into account to obtain an accurate analysis of hydrogel transient behavior.

Historically, the theoretical study of surface stresses in solids was presented in papers by Gurtin and Murdoch (1975, 1978) based on empirical observations of crystals. The Gurtin-Murdoch theory considers a 2D membrane bonded to the surface of a substrate material and includes a systematic theoretical framework for the tensorial nature of surface stresses using force and moment balance laws. This theory was later expanded by Steigmann and Ogden (1999) to consider the effects of intrinsic flexural resistance of the surface film to strain. Steinmann (2008) further expanded on Gurtin's theories on the configurational mechanics of surfaces. From a numerical perspective, Javili and Steinmann (2009), Javili and Steinmann (2010), Javili et al. (2014) and Henann and Bertoldi (2014) provided finite element framework for considering solid continua with surface effects at finite deformations.

Linear and nonlinear theories have been utilized to study the coupled deformation and kinetics of hydrated polymeric materials. Linear theories (Bouklas and Huang, 2012; Delavoipière et al., 2018; Okumura et al., 2020) have followed the classical theory of linear poroelasticity presented by Biot (1941). Recently they have been extended to consider elastocapillary effects (Liu et al., 2020a). For the quasi-static study of the elastomeric networks with a solvent Flory and Rehner (1943) utilized statistical mechanics to develop a free energy function that involves the configurational entropy of the mixture between solvent molecules and long polymers and the entropy of the network stretching. Recent non-linear theories that consider the effects of mass transport (solvent diffusion) and large deformations (Chester, 2012; Duda et al., 2010; Hong et al., 2008) have prominently used Darcy's law for incorporating diffusion. Several implementations of the nonlinear theories into finite element frameworks have also been presented (Chester et al., 2015; Bouklas et al., 2015b; Lucantonio et al., 2013).

The goal of this work is to extend the existing framework for studying the transient response of hydrogels to incorporate elastocapillary effects at finite deformations coupled with solvent diffusion. As a specific example we use the proposed method to analyze the problem of swelling microspheres with elastocapillary effects. The outline of this paper is as follows.

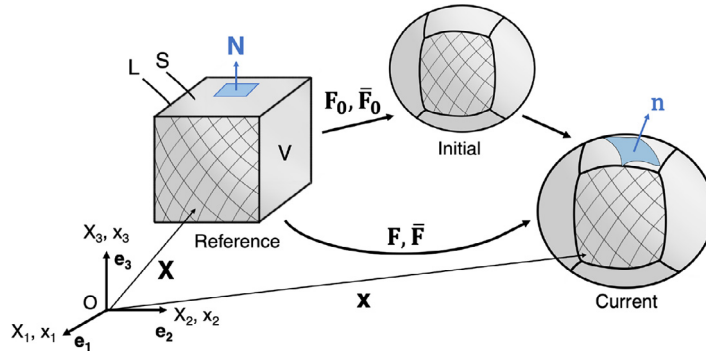


**Fig. 1.** Schematic illustration of the reference, initial, and current state of a continuum body. The initial state is assumed to be isotropically scaled from the reference state. The reference volume, surface, and boundary curve are denoted by  $V$ ,  $S$ , and  $L$  respectively. The normal vector to the surface is shown in the reference and current configuration ( $\mathbf{N}$  and  $\mathbf{n}$ ). Overbars indicate surface terms.

In [Section 2](#), we outline the nonlinear theory, including the kinematic definitions, the non-equilibrium thermodynamic theory, and the equations of state. In [Section 3](#), we present the mixed finite element formulation which is implemented in *FEniCS* ([Alnæs et al., 2015; Logg et al., 2012](#)). [Section 4](#) focuses on the linear theory and the development of a semi-analytical solution for the swelling response of hydrogel micro-spheres in the presence of surface stresses. [Section 5](#) states the normalizations of all equations and the initial and boundary conditions for our model before presenting results and discussion. We compare the results of the nonlinear theory to the linear theory for a free swelling micro-sphere with and without surface stresses. We discuss the microscopic origins of surface effects in hydrogels and propose a Neo-Hookean type surface free energy comparing the transient results to the latter case. Our finite element implementation is also utilized to show the transient response for more complex shapes and constrained swelling structures. Finally, we provide a discussion on the significant differences of swelling and drying kinetics in the presence of surface stresses. This phenomenon has not been addressed in other work previously and can have a profound effect on the design of drug delivery systems.

## 2. A Nonlinear Theory

In this section, we outline the non-equilibrium thermodynamic theory following [Hong et al. \(2008\)](#) and [Bouklas et al. \(2015b\)](#), and utilize Flory theory to obtain the equations of state for the spherical hydrogel ([Flory, 1953](#)). For a complete definition of key concepts for the kinematics of boundaries the reader is referred to [Green and Zerna \(1992\)](#), or [do Carmo \(1976\)](#). Some comprehensive works merging concepts of mechanics and differential geometry for the development of equilibrium theories are found in [Gurtin and Murdoch \(1975\)](#), [Steinmann \(2008\)](#), [Javili et al. \(2014\)](#), and [Liu et al. \(2020\)](#).

### 2.1. Kinematics

[Fig. 1](#) illustrates a continuum body,  $\mathcal{B}$ , in the reference (material), initial and current (spatial) configuration, where the initial state is not necessarily coincident with the reference state. The reference frame is a right-handed orthonormal coordinate system. The reference configuration of the continuum body is denoted by  $V$ , and the current configuration by  $v$ . When the current configuration coincides with the reference configuration, the body is stress free.

To denote reference and current coordinates, we use  $\mathbf{X} \in V$  and  $\mathbf{x} \in v$  respectively. The displacement,  $\mathbf{u}$ , is defined by  $\mathbf{u} = \mathbf{x} - \mathbf{X}$ . Taking the gradient of this expression defines the invertible deformation map,  $\mathbf{x} = \varphi(\mathbf{X})$ , which we can denote by,  $\varphi : V \rightarrow \mathbb{R}^3$ . The kinematics of an infinitesimal material line element are described by the deformation gradient, which maps the reference configuration  $\mathbf{X}$  to the current configuration  $\mathbf{x}$ .

$$\mathbf{F}(\mathbf{X}, t) = \frac{\partial \varphi(\mathbf{X}, t)}{\partial \mathbf{X}} = \nabla_{\mathbf{X}} \mathbf{x}(\mathbf{X}, t) \quad (2.1a)$$

$$\mathbf{F}^{-1}(\mathbf{x}, t) = \frac{\partial \varphi^{-1}(\mathbf{x}, t)}{\partial \mathbf{x}} = \nabla_{\mathbf{x}} \mathbf{X}(\mathbf{x}, t) \quad (2.1b)$$

where  $\mathbf{F}(\mathbf{X}, t)$  and  $\mathbf{F}^{-1}(\mathbf{x}, t)$  are the deformation gradient and inverse deformation gradient, respectively.

In [Fig. 1](#), a motion of an arbitrary differential vector element can be mapped by the deformation gradient  $\mathbf{F}$ . However, a unit normal vector  $\mathbf{N}$  in the reference configuration cannot be transformed into a unit normal vector  $\mathbf{n}$  in the current configuration via the deformation gradient, motivating us to develop the kinematics of an infinitesimal surface element ([Holzapfel, 2000; Steinmann, 2008](#)),

$$\bar{\mathbf{F}}(\bar{\mathbf{X}}, t) = \frac{\partial \varphi(\bar{\mathbf{X}}, t)}{\partial \bar{\mathbf{X}}} \cdot \bar{\mathbf{I}} = \bar{\nabla}_{\bar{\mathbf{X}}} \bar{\mathbf{x}}(\bar{\mathbf{X}}, t) \quad (2.2a)$$

$$\bar{\mathbf{F}}^{-1}(\bar{\mathbf{x}}, t) = \frac{\partial \varphi^{-1}(\bar{\mathbf{x}}, t)}{\partial \bar{\mathbf{x}}} \cdot \bar{\mathbf{i}} = \bar{\nabla}_{\bar{\mathbf{x}}} \bar{\mathbf{X}}(\bar{\mathbf{x}}, t) \quad (2.2b)$$

where  $\bar{\mathbf{F}}(\bar{\mathbf{X}}, t)$  and  $\bar{\mathbf{F}}^{-1}(\bar{\mathbf{x}}, t)$  are the surface deformation gradient and inverse surface deformation gradient respectively. The mixed variant surface identity tensor is denoted in the reference and the current configuration as  $\bar{\mathbf{I}}$  and  $\bar{\mathbf{i}}$ , respectively. Note that the surface deformation gradient can be defined in relation to the bulk deformation gradient, Eq. (2.1),  $\bar{\mathbf{F}} = \mathbf{F} \cdot \bar{\mathbf{I}}$ .

The Jacobian determinant describes the volumetric ratio between the reference and current configurations,  $J(\mathbf{X}, t) = \det \mathbf{F}(\mathbf{X}, t) = dv/dV > 0$ . Just as how the bulk Jacobian describes the volumetric change, the surface Jacobian,  $\bar{J}$  describes the surface area change by mapping the surface element in the reference,  $dS$ , to the surface element in the current coordinates,  $ds$ ,  $\bar{J} = \det \bar{\mathbf{F}} = ds/dS$ .

## 2.2. Equilibrium and Constitutive Relationships

In the following derivation, we start at the equilibrium equations and derive the equations of state. Alternatively as demonstrated in Javili and Steinmann (2009, 2010) the total potential energy densities of the bulk and surface can be minimized with respect to the admissible variations in order to obtain the localized force balances and equations of state. In the field theory of gels, there is both mechanical and chemical work done (Hong et al., 2008). The surface,  $S$ , of the continuum body,  $B$ , is composed of subregions,

$$S = S^u \cup S^T = S^\mu \cup S^i \quad (2.3a)$$

$$0 = S^u \cap S^T = S^\mu \cap S^i \quad (2.3b)$$

where the superscript in  $S^{(\cdot)}$  indicates the quantity prescribed in the specific subregion from the work conjugate pairs of displacement and traction ( $u$  and  $T$ ) and chemical potential and surface flux ( $\mu$  and  $i$ ).

Mechanical equilibrium is maintained, following Steinmann (2008). The localized force balance within the volume,  $V$ , the surface,  $S$ , and the boundary curves,  $L$ , is

$$\nabla_X \cdot \mathbf{P} + \mathbf{b}_0 = 0 \quad \text{in } V \quad (2.4a)$$

$$\mathbf{P} \cdot \mathbf{N} - \bar{\nabla}_X \cdot \bar{\mathbf{P}} = \check{\mathbf{T}} \quad \text{on } S^T \quad (2.4b)$$

$$\mathbf{u} = \check{\mathbf{u}} \quad \text{on } S^u \quad (2.4c)$$

$$[[\bar{\mathbf{P}} \cdot \bar{\mathbf{N}}]] = 0 \quad \text{on } L \quad (2.4d)$$

where  $\mathbf{P}$  is the 1st Piola-Kirchhoff (PK) stress,  $\bar{\mathbf{P}}$  is the surface 1st PK stress,  $\mathbf{b}_0$  is the body force, and  $\mathbf{T}$  is the traction force. Boundary conditions follow from Javili and Steinmann (2010), where we use  $(\check{\cdot})$  to indicate a prescribed value on the given boundary.  $\bar{\mathbf{N}}$  indicates the binormal vector to the boundary curve,  $L$ . The double brackets indicate summation over the two surfaces that intersect on the boundary curve. Eq. (2.4)d states that the component of surface stress normal to the boundary curve is continuous between adjacent surfaces, physically corresponding to the smoothing of sharp boundary edges.

Through mass conservation, an equation for the rate of change of nominal solvent concentration,  $\dot{C}$  is given as

$$\dot{C} + \nabla_X \cdot \mathbf{J} = r \quad \text{in } V \quad (2.5a)$$

$$\mathbf{J} \cdot \mathbf{N} = -i \quad \text{on } S^i \quad (2.5b)$$

$$\mu = \check{\mu} \quad \text{on } S^\mu \quad (2.5c)$$

where  $\mathbf{J}$  indicates the nominal flux of the solvent in the reference configuration,  $r$  and  $i$  are source terms for the number of solvent molecules traveling into a unit reference volume or into a unit surface area per unit time respectively, and  $\mu$  is the chemical potential.

The surface of a body is microscopically distinct from the bulk; therefore, the free energy density of a material volume element is denoted by  $U(\mathbf{F}, \mu)$  and the excess free energy density of a surface element is denoted by  $\bar{U}(\bar{\mathbf{F}})$ . Following the theory set forth in Hong et al. (2008) and Bouklas et al. (2015b), the bulk strain energy density is obtained in terms of the deformation gradient and the chemical potential through a Legendre transform.

$$U(\mathbf{F}, \mu) = U_e(\mathbf{F}) + U_m(C) - \mu C, \quad \bar{U}(\bar{\mathbf{F}}) = u_e(\bar{\mathbf{F}}) \quad (2.6)$$

where  $U_e$  is the free energy due to elastic stretching and  $U_m$  is the contribution due to polymer-solvent mixing. Here, we assume that the energy contribution from the boundary only includes an elastic term,  $u_e$ , and is dependent on the surface deformation gradient,  $\bar{\mathbf{F}}$ , neglecting mixing contributions. This assumption considers that the free energy contribution of the surface is just due to the stretching of the elastomeric component of the hydrogel and is not a function of concentration. This choice follows from experimental works that demonstrate that the polymeric constituents can be responsible for the rise of significant surface effects without the presence of solvent as discussed in Bico et al. (2018). Surface effects in hydrogels have

been experimentally verified (Hui et al. 2002; Mora et al. 2013), but a more detailed experimental investigation on surface effects on diffusion has not been performed. Therefore, we do not take into account more complex phenomena that could potentially take place, for example, surface diffusion (McBride et al., 2011) or chemical coupling under the condition of local equilibrium.

The variation of the free energy density of a volume and a surface element,  $\delta U$  and  $\delta \bar{U}$ , associated with small changes in the deformation gradient,  $\delta \mathbf{F}$ , surface deformation gradient,  $\delta \bar{\mathbf{F}}$ , and the chemical potential  $\delta \mu$  is as follows.

$$\delta U(\mathbf{F}, \mu) = \frac{\partial U(\mathbf{F}, \mu)}{\partial \mathbf{F}} \delta \mathbf{F} + \frac{\partial U(\mathbf{F}, \mu)}{\partial \mu} \delta \mu, \quad \delta \bar{U}(\bar{\mathbf{F}}) = \frac{\partial u_e(\bar{\mathbf{F}})}{\partial \bar{\mathbf{F}}} \delta \bar{\mathbf{F}} \quad (2.7)$$

The free energy of the system,  $G$ , which consists of the surface and bulk free energy contributions of the material and the potential energy of the weights and pumps acting on the system, changes at the rate,

$$\dot{G} = \int_V \frac{\delta U}{\delta t} dV + \int_S \frac{\delta \bar{U}}{\delta t} dS - \int_V \mathbf{b}_0 \frac{\delta \mathbf{x}}{\delta t} dV - \int_V \mu r dV - \int_S \mu i dS - \int_S \check{\mathbf{T}} \frac{\delta \check{\mathbf{x}}}{\delta t} dS \quad (2.8)$$

where  $\int_V \mu r dV + \int_S \mu i dS$  is the rate of chemical work and  $\int_V \mathbf{b}_0 (\delta \mathbf{x} / \delta t) dV + \int_S \check{\mathbf{T}} (\delta \check{\mathbf{x}} / \delta t) dS$  are related to the rate of mechanical work.

Following Hong et al. (2008), we use Eq. (2.5) for the mass conservation, and Eq. (2.7) for the rate of change of the total free energy to obtain the following expression combining the bulk and surface contributions,

$$\dot{G} = \int_V \left( \frac{\partial U}{\partial \mathbf{F}} - \mathbf{P} \right) \frac{\delta \mathbf{F}}{\delta t} dV + \int_S \left( \frac{\partial \bar{U}}{\partial \bar{\mathbf{F}}} - \bar{\mathbf{P}} \right) \frac{\delta \bar{\mathbf{F}}}{\delta t} dS + \int_V \left( \frac{\partial U}{\partial \mu} + C \right) \frac{\delta \mu}{\delta t} dV + \int_V \mathbf{J} \cdot \frac{\partial \mu}{\partial \mathbf{x}} dV \quad (2.9)$$

Each integral represents a distinct mechanism of energy dissipation. The first and second integral represent the local re-arrangement of small molecules in the bulk and surface respectively, the third integral represents the chemical work, and the last integral indicates the work of time-dependent long-range diffusion of solvent molecules. Applying the second law of thermodynamics (the Clausius-Plank Inequality) that states that the free energy of the system should never increase,  $\delta G / \delta t \leq 0$ , ensures that each integral must either be negative or zero. Following the Coleman-Noll procedure, we obtain the expressions for the 1st PK stress, the surface 1st PK stress, and the solvent concentration.

$$\mathbf{P} = \frac{\partial U}{\partial \mathbf{F}}, \quad \bar{\mathbf{P}} = \frac{\partial \bar{U}}{\partial \bar{\mathbf{F}}}, \quad C = -\frac{\partial U}{\partial \mu} \quad (2.10)$$

In order to ensure that the last integrand of Eq. (2.9) is negative definite, we adopt a kinetic law where the mobility tensor,  $\mathbf{M}$ , is symmetric and positive definite (Hong et al., 2008).

$$\mathbf{J} = -\mathbf{M} \cdot \nabla \mu \quad \text{where} \quad \mathbf{M} = \frac{CD}{k_B T} \mathbf{F}^{-1} \mathbf{F}^{-T} \quad (2.11)$$

$D$  is the intrinsic diffusion coefficient, describing the diffusivity of a solvent molecule in the solvent,  $k_B$  is Boltzmann's constant, and  $T$  is the temperature.

### 2.3. A Specific Free Energy: Volume and Surface

The free energy of elastic stretching of the network of polymer chains by Flory (1953) is

$$U_e(\mathbf{F}) = \frac{1}{2} N k_B T [\text{tr} \mathbf{C} - 3 - 2 \log(\det \mathbf{F})] \quad (2.12)$$

where  $N$  is the effective number of polymer chains per unit volume of the polymer and  $\mathbf{C} = \mathbf{F}^T \mathbf{F}$  is the right Cauchy-Green tensor. The free energy of polymer-solvent mixing is defined as (Flory, 1953; Huggins, 1941)

$$U_m(C) = -\frac{k_B T}{\Omega} \left[ \Omega C \log\left(\frac{1 + \Omega C}{\Omega C}\right) + \frac{\chi}{1 + \Omega C} \right] \quad (2.13)$$

where  $\Omega$  is the volume of a solvent molecule. The Flory parameter,  $\chi$ , also known as the interaction parameter, governs how likely solvent molecules are to enter or leave the hydrogel based on interaction between the solvent and the polymer.

Surface effects are considered through the introduction of a surface free energy, leading to a constitutive law for the surface-stress. For clarification, note that the terms surface energy and surface tension are used interchangeably in the case

of liquids, but this is not generally true for surface energy and surface stress in solids (Javili and Steinmann, 2009, 2010; Style et al., 2017). We consider both a fluid-like surface energy and a Neo-Hookean type surface free energy. First a fluid-like model assumes a constant surface energy per unit deformed area,  $\gamma$ , which we define in the reference configuration as

$$\bar{U}(\bar{\mathbf{F}}) = \gamma \bar{J} \quad (2.14)$$

where  $\bar{J}$  is the ratio of current to reference surface area.

A second option is to assume a Neo-Hookean surface response given the nature of the polymeric material. The surface free energy density in this case can be expressed as,

$$\bar{U}(\bar{\mathbf{F}}) = \frac{\lambda_b}{2} \log^2 \bar{J} + \frac{\mu_b}{2} (\bar{\mathbf{F}} : \bar{\mathbf{F}} - 2 - 2 \log \bar{J}) \quad (2.15)$$

where  $\lambda_b$  is the area modulus and  $\mu_b$  is the surface shear modulus (Javili and Steinmann, 2010).

We assume that the hydrogel volume changes occur only through solvent diffusion

$$\det(\mathbf{F}) = 1 + \Omega C \rightarrow C = \frac{\det(\mathbf{F}) - 1}{\Omega} \quad (2.16)$$

considering that the hydrogel constituents are individually incompressible. This expression allows us to write  $U$  from Eq. (2.6) as a function of chemical potential and the deformation gradient and leads to the chemical potential  $\mu$  acting as a Lagrange multiplier to enforce the constraint from Eq. (2.16) in Eq. (2.6) as shown previously in Bouklas et al. (2015a).

The expression for the 1st PK stress can be calculated from Eq. (2.10) using the free energy of stretching,

$$\mathbf{P} = Nk_B T (\mathbf{F} + \alpha \mathbf{F}^{-T}) \quad (2.17)$$

where  $\alpha$  is

$$\alpha = -\frac{1}{\det \mathbf{F}} + \frac{1}{N\Omega} \left[ \frac{1}{\det \mathbf{F}} + \log \left( \frac{\det \mathbf{F} - 1}{\det \mathbf{F}} \right) + \frac{\chi}{(\det \mathbf{F})^2} - \frac{\mu}{k_B T} \right] \quad (2.18)$$

The surface 1st PK stress tensors for the fluid-like surface free energy and the Neo-Hookean surface free energy respectively are given as,

$$\bar{\mathbf{P}} = \gamma \bar{J} \bar{\mathbf{F}}^{-T} \quad (2.19a)$$

$$\bar{\mathbf{P}} = \lambda_b \log \bar{J} \bar{\mathbf{F}}^{-T} + \mu_b (\bar{\mathbf{F}} - \bar{\mathbf{F}}^{-T}) \quad (2.19b)$$

We note that the former expression would lead to a constant Cauchy surface stress as pointed out in Javili and Steinmann (2010).

### 3. Finite Element Implementation

#### 3.1. Variational Formulation

In order to fully define the strong form Eq. (2.4) & (2.5), a set of initial conditions need to be prescribed in combination with Eqs. (2.4) and (2.5). Initial conditions are prescribed in terms of displacements  $\mathbf{u}$ , and the chemical initial conditions are prescribed in terms of the chemical potential,  $\mu$ .

$$\mathbf{u}|_{t=0} = \mathbf{u}_0 \quad (3.1a)$$

$$\mu|_{t=0} = \mu_0 \quad (3.1b)$$

The pair of trial functions spaces corresponding to  $\mathbf{u}(\mathbf{X}, t)$  and  $\mu(\mathbf{X}, t)$  are defined as

$$Q_{\mathbf{u}} = \mathbf{u} : V \rightarrow \mathbb{R}^3 \mid \mathbf{u} \in \mathbf{H}^1, \quad \mathbf{u} = \tilde{\mathbf{u}} \quad \text{on } S^u \quad (3.2a)$$

$$Q_{\mu} = \mu : V \rightarrow \mathbb{R} \mid \mu \in \mathbf{H}^1, \quad \mu = \tilde{\mu} \quad \text{on } S^{\mu} \quad (3.2b)$$

with  $\mathbf{H}^1$  denoting Sobolev spaces of degree one. For the test functions  $\delta \mathbf{u}(\mathbf{X})$  and  $\delta \mu(\mathbf{X})$  equivalent spaces can be defined satisfying homogeneous conditions on the essential boundaries as

$$Q_{\delta \mathbf{u}} = \delta \mathbf{u} : V \rightarrow \mathbb{R}^3 \mid \delta \mathbf{u} \in \mathbf{H}^1, \quad \delta \mathbf{u} = \mathbf{0} \quad \text{on } S^u \quad (3.3a)$$

$$Q_{\delta \mu} = \delta \mu : V \rightarrow \mathbb{R} \mid \delta \mu \in \mathbf{H}^1, \quad \delta \mu = 0 \quad \text{on } S^{\mu} \quad (3.3b)$$

The weak form of the problem is now to find  $[\mathbf{u}, \mu] \in Q_{\mathbf{u}} \times Q_{\mu}$ , such that for any  $[\delta \mathbf{u}, \delta \mu] \in Q_{\delta \mathbf{u}} \times Q_{\delta \mu}$ , the following holds,

$$G(\mathbf{u}, \mu, \delta \mathbf{u}) = \int_S \bar{\mathbf{P}} \cdot \bar{\nabla}_{\mathbf{X}} \delta \mathbf{u} dS + \int_V \mathbf{P} \cdot \nabla_{\mathbf{X}} \delta \mathbf{u} dV - \int_S \check{\mathbf{T}} \cdot \delta \mathbf{u} dS - \int_V \mathbf{b}_0 \cdot \delta \mathbf{u} dV = 0 \quad (3.4a)$$

$$H(\mathbf{u}, \mu, \delta \mu) = \int_V \dot{C} \delta \mu dV - \int_V \mathbf{J} \cdot \nabla_{\mathbf{X}} \delta \mu dV - \int_V r \delta \mu dV - \int_S i \delta \mu dS = 0 \quad (3.4b)$$



### 3.2. Temporal and spatial discretization

It follows that the second expression in Eq. (3.4) can be discretized in time by employing the backwards Euler method, which gives

$$H(\mathbf{u}, \mu, \delta\mu) = \int_V (C - C^t) \delta\mu dV - \int_V \mathbf{J} \cdot \frac{\delta\mu}{\delta X} \Delta t dV - \int_S i \delta\mu \Delta t dS - \int_V r \delta\mu \Delta t dV = 0. \quad (3.5)$$

where the superscript  $t$  indicates values at the previous time iteration and no superscript indicates the current time iteration. The time step of the scheme is indicated as  $\Delta t$ .

A mixed finite element method is utilized to solve for the displacement and chemical potential fields concurrently. In order to produce numerically stable results with the mixed method, which are known to arise due to the saddle-point nature of the mixed scheme, we employ proper spatial discretization techniques to not violate the Ladyzhenskaya-Bubuka-Brezzi (LBB) condition (Krischok and Linder, 2019; Sun et al., 2013). In this work (following Bouklas et al. (2015b)) we use the lowest order Taylor-Hood space where the interpolation for displacement is quadratic, and the interpolation for the chemical potential is linear.

$$\mathbf{u} = \mathbf{N}^u \mathbf{u}^n, \quad \mu = \mathbf{N}^\mu \mu^n \quad (3.6)$$

$\mathbf{N}^u$  and  $\mathbf{N}^\mu$  are shape functions for displacement and chemical potential respectively. The nodal values for the displacement and chemical potential are  $\mathbf{u}^n$  and  $\mu^n$  respectively. Discretization of the test functions is carried out in the same manner

$$\delta\mathbf{u} = \mathbf{N}^u \delta\mathbf{u}^n, \quad \delta\mu = \mathbf{N}^\mu \delta\mu^n \quad (3.7)$$

Taking the gradients of Eq. (3.6) for calculation of the 1st PK stress, surface PK stress, solvent concentration, and flux at the integration points,

$$\nabla_X \mathbf{u} = \nabla_X \mathbf{N}^u \delta\mathbf{u}^n = \mathbf{B}^u \mathbf{u}^n \quad (3.8a)$$

$$\nabla_X \mu = \nabla_X \mathbf{N}^\mu \delta\mu^n = \mathbf{B}^\mu \mu^n \quad (3.8b)$$

where  $\mathbf{B}^u$  and  $\mathbf{B}^\mu$  are the gradients of the shape functions for displacement and chemical potential respectively.

### 3.3. Nonlinear solution

After the appropriate discretizations, the weak form from Eqs. (3.4) and (3.5) can be expressed as a global system of nonlinear equations. This system can be solved iteratively using the Newton-Raphson method at each time step, where the residual,  $R$ , must be set to zero to solve for the displacements and chemical potentials,  $\mathbf{d} = [\mathbf{u}^n \quad \mu^n]^T$ , at each node.

$$R(\mathbf{d}, \delta\mathbf{d}) = G(\mathbf{u}, \mu, \delta\mathbf{u}) + H(\mathbf{u}, \mu, \delta\mu) = 0 \quad (3.9)$$

$G$  and  $H$  contain known quantities, the body and traction forces, the prescribed source terms, and the known concentration from the  $i$ th iteration. The correction to the solution at the  $i$ th iteration is defined as  $\delta\mathbf{d}_i$ :

$$\delta\mathbf{d}_i = \left[ \frac{\partial \mathbf{R}}{\partial \mathbf{d}} \Big|_{\mathbf{d}_i} \right]^{-1} \mathbf{R}_i \quad (3.10)$$

where the nodal unknowns are updated at each iteration,  $\delta d_i = d_{i+1} - d_i \rightarrow d_{i+1} = d_i + \delta d_i$ . Eq. (3.10) requires the calculation of the tangent Jacobian matrix at each iteration,

$$\frac{\partial \mathbf{R}}{\partial \mathbf{d}} \Big|_{\mathbf{d}_i} = \begin{bmatrix} \mathbf{K}^{uu} & \mathbf{K}^{u\mu} \\ \mathbf{K}^{\mu u} & \mathbf{K}^{\mu\mu} \end{bmatrix} \quad (3.11)$$

The coupled non-linear equations are solved numerically in FEniCS version 2019.1.0 via the Portable Extensible Toolkit for Scientific Computations' (PETSc) Scalable Nonlinear Equations Solvers (SNES) interface. This process repeats until a level of convergence specified within the SNES solver.

## 4. Linear theory: Microsphere solution

Insight can be gained by studying the special case of a swollen microsphere exposed to a solvent at a slightly different chemical potential,  $\mu$ , from its initial equilibrium chemical potential value,  $\mu_0$ . In the dry state, the sphere has radius,  $A$ . After free swelling, the radius increases to  $a_0 = \lambda_0 A$ , where  $\lambda_0$  is the stretch ratio due to swelling. We assume constant surface stress,  $\gamma$ , and consider the limiting case where the change in chemical potential,  $\mu - \mu_0$ , is sufficiently small so the resulting deformation can be modeled accurately by the linearized theory of poroelasticity (Biot, 1941; McNamee and Gibson, 1960; Rice and Cleary, 1976; Bouklas and Huang, 2012; Liu et al. 2020c). Bouklas and Huang (2012) has shown that the difference in chemical potential corresponds to imposing a pore pressure,  $p^*$  on the surface of the sphere,

$$p^* = -\frac{\mu - \mu_0}{\Omega} \quad (4.1)$$

where we use the convention that a positive pore pressure corresponds to hydrostatic tension (Hui et al., 2006; Scherer, 1989). We linearize the swollen state where the pore pressure is initially zero inside the gel and then at  $t = 0^+$ , the sphere is exposed to the solvent in which the pore pressure is  $p^*$ . For time  $t = 0$ , the true stress is hydrostatic and the Laplace pressure is  $\sigma_0 = -2\gamma/a_0$ . In the following, all the strain and displacement fields are measured from the swollen state where  $\mu = \mu_0$ . The pore pressure field inside the gel is denoted by  $p(r, t)$ . We use a spherical coordinate system  $(r, \theta, \phi)$  with an origin at the center of the sphere. Due to symmetry, only the radial displacement,  $u$ , is non-zero and the non-trivial strains fields are principal and related to the displacement

$$\varepsilon_\theta = \varepsilon_\phi = \frac{u}{r}, \quad \varepsilon_r = \frac{\partial u}{\partial r} \quad (4.2)$$

The linearized constitutive model, in spherical coordinates, is Biot (1941)

$$\sigma_r = \frac{(4G_0 + 3K_0)\varepsilon_r + (6K_0 - 4G_0)\varepsilon_\theta}{3} + p \quad (4.3a)$$

$$\sigma_\theta = \sigma_\phi = \frac{(-2G_0 + 3K_0)\varepsilon_r + (6K_0 + 2G_0)\varepsilon_\theta}{3} + p \quad (4.3b)$$

where  $\sigma_r$ ,  $\sigma_\theta$ , and  $\sigma_\phi$  are the incremental stresses. The bulk and shear modulus of the network are  $K_0$  and  $G_0$  respectively, and are related by  $3K_0 = 2G_0(1 + \nu)/(1 - 2\nu)$ , where  $\nu$  is the Poisson's ratio of the network. Poisson's ratio is related to the swelling ratio,  $\lambda_0$ , as shown in Bouklas and Huang (2012)

$$\nu = \frac{1}{2} - \frac{N\Omega}{2} \left[ \frac{1}{\lambda_0^2(\lambda_0^3 - 1)} + \frac{N\Omega}{\lambda_0^2} - \frac{2\chi}{\lambda_0^5} \right]^{-1} \quad (4.4)$$

For notational simplicity, we have not included the hydrostatic stress due to Laplace pressure,  $\sigma_0$ , in Eq. (4.3), hence the stresses  $\sigma_r$ ,  $\sigma_\theta$ , and  $\sigma_\phi$  are incremental stresses. In other words, the actual true stress after the gel is exposed to solvent is  $\sigma_0 + \sigma_r$ ,  $\sigma_0 + \sigma_\theta$ , and  $\sigma_0 + \sigma_\phi$ . The non-trivial equilibrium equation is

$$\frac{\partial \sigma_r}{\partial r} + \frac{2(\sigma_r - \sigma_\theta)}{r} = 0 \quad (4.5)$$

Darcy's law in linear poroelasticity can be written as,

$$\frac{k}{\eta} \nabla_x^2 p = -\frac{\partial e}{\partial t} \quad (4.6)$$

where  $e$  is the volumetric strain  $e = u_{,r} + 2u/r$ . The coefficient of permeability,  $k$ , and the fluid viscosity,  $\eta$ , connect to the initial mobility,  $M_0$ , of an isotropically swollen gel (Bouklas and Huang, 2012)

$$M_0 = \frac{k}{\eta \Omega^2} = \frac{D}{\Omega k_B T} \frac{\lambda_0^3 - 1}{\lambda_0^3} \quad (4.7)$$

Eqs. (4.2) to (4.6) are the governing equations for the microsphere problem. These governing equations are to be solved with the following initial and boundary conditions:

$$p(r = a_0, t > 0) = p^*, \quad \sigma_r(r = a_0, t > 0) = 0 \quad (4.8a)$$

$$p(r < a_0, t = 0) = 0, \quad \sigma_r(r < a_0, t = 0) = \sigma_\theta(r < a_0, t = 0) = 0 \quad (4.8b)$$

Using compatibility and equilibrium, we show that the circumferential strain and the radial stress are related by (See Appendix A for full details),

$$\varepsilon_\theta = -\frac{\sigma_r}{4G_0} + f(t) \quad (4.9)$$

where  $f(t)$  is only a function of time. Substituting Eq. (4.9) into (4.3a), we obtain

$$\frac{1}{2G_0} \sigma_r = \varepsilon_r + \frac{(6K_0 - 4G_0)}{(4G_0 + 3K_0)} f(t) + \frac{3}{4G_0 + 3K_0} p \quad (4.10)$$

The volumetric strain  $e$  is obtained by eliminating  $\sigma_r$  from Eqs. (4.9) and (4.10), i.e.,

$$e = \frac{12G_0}{(4G_0 + 3K_0)} f(t) - \frac{3}{4G_0 + 3K_0} p \quad (4.11)$$

Substituting Eq. (4.11) into Darcys law, Eq. (4.6), we obtain

$$\frac{\partial p}{\partial t} - k \frac{4G_0 + 3K_0}{3\eta} \nabla_x^2 p = 4G_0 f'(t) \quad (4.12)$$



The radial stress can be obtained using compatibility,  $\varepsilon_r = (r\varepsilon_\theta)_{,r}$ , Eqs. (4.10) and (4.3) (See Appendix A for full details); this results in:

$$\sigma_r = \frac{\Lambda_2}{r^3} \int_0^r q^2 p(q, t) dq + \frac{\Lambda_1 f(t)}{3} \quad \text{where} \quad \Lambda_1 = \frac{36K_0 G_0}{(4G_0 + 3K_0)}, \quad \Lambda_2 = \frac{12G_0}{4G_0 + 3K_0} \quad (4.13)$$

The circumferential stress can be obtained from the equilibrium equation once the radial stress is known. We have therefore reduced the problem to solving for the pore pressure and  $f(t)$ . To determine  $f(t)$ , we impose the boundary condition

$$\sigma_r(r = a_0, t) = 0 \Rightarrow \frac{\Lambda_2}{a_0^3} \int_0^{a_0} q^2 p(q, t) dq + \frac{\Lambda_1 f(t)}{3} = 0 \quad (4.14)$$

Note Eq. (4.14) relates the radial stress to the pore pressure and the unknown function of time,  $f(t)$ . This is how the stress is coupled to diffusion. Furthermore, since we know that  $\sigma_r$ ,  $\sigma_\theta$  and the pore pressure field are identically zero at  $t = 0$ ,  $f(t = 0) = 0$ .

#### 4.1. Solutions and Normalizations

Stresses and pore pressure are normalized by the shear modulus,  $G_0$ . Lengths are normalized by  $a_0$ ,

$$\Sigma_r = \frac{\sigma_r}{G_0}, \quad P = \frac{p}{G_0}, \quad R = \frac{r}{a_0} \quad (4.15)$$

Time is normalized by  $3a_0^2\eta/k(4G_0 + 3K_0)$ , and denoted by  $\hat{T}$  to prevent confusion with the notation for temperature,

$$\hat{T} = \frac{k(4G_0 + 3K_0)t}{3a_0^2\eta} \quad (4.16)$$

Using these normalized variables, the diffusion equation, Eq. (4.12), becomes:

$$\frac{\partial P}{\partial \hat{T}} - \frac{1}{R^2} \frac{\partial}{\partial R} \left( R^2 \frac{\partial P}{\partial R} \right) = 4 \frac{df}{d\hat{T}} \quad (4.17)$$

The boundary and initial condition for Eq. (4.17) is

$$P(R, \hat{T} = 0^-) = 0 \quad (4.18a)$$

$$P(R = 1, \hat{T} > 0) = P^* \equiv \frac{p^*}{G_0} \quad (4.18b)$$

The normalized radial stress, Eq. (4.13), is

$$\Sigma_r = \frac{\Lambda_2}{R^3} \int_0^R q^2 P(q, t) dq + \frac{\hat{\Lambda}_1 f(\hat{T})}{3} \quad \text{where} \quad \hat{\Lambda}_1 = \frac{36K_0}{(4G_0 + 3K_0)} \quad (4.19)$$

The condition that traction vanishes at  $R = 1$  is

$$\Lambda_2 \int_0^1 q^2 P(q, t) dq = -\frac{\hat{\Lambda}_1 f(\hat{T})}{3} \quad (4.20)$$

In Appendix A, we show that the solution of Eq. (4.17) is,

$$P = P^* + \frac{1}{R} \sum_{n=1}^{\infty} \sin(n\pi R) H_n(\hat{T}) \quad \text{where} \quad (4.21)$$

$$H_n(\hat{T}) = \frac{8(-1)^{n+1}}{\pi n} \int_0^{\hat{T}} e^{-n^2\pi^2(\hat{T}-\hat{T}')} \frac{df}{d\hat{T}'} d\hat{T}' - \frac{2(-1)^{n+1}P^*}{\pi n} e^{-n^2\pi^2\hat{T}}$$

Next, we use Eq. (4.20) to determine the unknown function  $f$ . Substituting Eq. (4.21) into Eq. (4.20) results in a linear Volterra integral equation for  $f$ , i.e.,

$$\sum_{n=1}^{\infty} \left[ \frac{8}{n^2\pi^2} \int_0^{\hat{T}} \frac{df}{d\hat{T}'} e^{-n^2\pi^2(\hat{T}-q)} dq - P_0 \frac{2}{n^2\pi^2} e^{-n^2\pi^2\hat{T}} \right] = -\frac{\hat{\Lambda}_1 f(\hat{T})}{3\Lambda_2} - \frac{P^*}{3} \quad (4.22)$$

In theory, Eq. (4.22) can be solved using Laplace transform, but inversion in close form is not possible, so it is solved numerically with the condition  $f(\hat{T} = 0) = 0$ . Once  $f$  is determined,  $P$  is obtained using Eq. (4.21) and the stresses can be determined using Eq. (4.19) and the equilibrium equation.

## 5. Results and Discussion

We consider the swelling kinetics for three sets of initial boundary value problems: free swelling (and drying) of a sphere, free swelling of a cube, and constrained swelling of a cube, all immersed in solvent. All finite element models are implemented in FEniCS. Meshes are created in Gmsh (version 4.4.1), an open source 3D finite element mesh generator (Geuzaine and Remacle, 2009). In the three numerical cases, we take  $N\Omega = 10^{-3}$  and use low  $\chi$  values from the range 0.2 to 0.6 indicating a hydrophilic response of the polymeric network to the specific solvent. For the simulations, the initial time step is set to  $\Delta t = 10^{-5}$ , and is exponentially increased until equilibrium is reached. For the case of a hydrogel sphere swelling and drying we compare the solution of the linear theory to the finite element results.

### 5.1. Normalizations

For the finite element simulations, all parameters are normalized, as denoted by  $\hat{\phantom{x}}$ , following from the non-linear theory. Lengths are normalized by a referential (dry-state and undeformed) dimension,  $A$ . In the equivalent cases,  $A$  will denote the radius of the sphere and the length of the edge of the cube. Surface energy, bulk and surface stresses, and chemical potential are normalized respectively by,

$$\hat{\gamma} = \frac{\gamma}{Nk_B T A}, \quad \hat{\mathbf{P}} = \frac{\mathbf{P}}{Nk_B T}, \quad \hat{\mu} = \frac{\mu}{k_B T} \quad (5.1)$$

Solvent concentration and time are normalized as follows,

$$\hat{C} = C\Omega, \quad \hat{t} = \frac{Dt}{A^2}. \quad (5.2)$$

For diffusion problems, time is normalized by the characteristic diffusion time-scale,  $A^2/D$ . For comparisons between the linear microsphere theory and the simulations, the results from the linear microsphere solution are re-normalized using finite element simulation normalizations.

In the following Sections 5.2.1 and 5.2.2, we will discuss in detail the implications of choosing a constant surface free energy and a Neo-Hookean surface energy (in the current configuration). For the former case, we define the elastocapillary length-scale as  $l = \gamma/G_0$ , and the dimensionless elastocapillary number as  $n_{ec} = \gamma\bar{\kappa}/G_0$ . The instantaneous shear modulus is defined, Bouklas and Huang (2012)

$$G_0 = \frac{Nk_B T}{\lambda_0} \quad (5.3)$$

In the case of a homogeneously swollen sphere with constant surface free energy, the normalized elastocapillary length scale is given as  $\hat{l} = l/A = \hat{\gamma}A\lambda_0$ .

### 5.2. Free Swelling and Drying of a Sphere

Here, we consider free swelling of a sphere. The sphere is at an initial homogeneously swollen state with initial stretch  $\lambda_0$  and initial chemical potential  $\hat{\mu}_0$ . The sphere can reach the initial swollen state in various ways; namely, being synthesized with an initial concentration of solvent or being in an humid environment for an extended period of time. Following the initial state, the sphere is immersed in solvent such that the chemical potential boundary condition  $\hat{\mu} = 0$  on the complete outer surface of the sphere is  $S^\mu = S$ . The sphere is traction free, but constrained to remove rigid body motions.

Determining the initial condition of the system is not straightforward like the case with no surface effects. Given an initial homogeneous swelling stretch  $\lambda_0$ , the initial chemical potential  $\hat{\mu}_0$  is not known, and vice-versa. In the case of a constant surface energy per unit deformed area, an analytical expression connecting initial chemical potential  $\hat{\mu}_0$  and initial stretch  $\lambda_0$  can be determined (discussed in Appendix B). In the case of the Neo-Hookean surface energy an additional ramping procedure has to be considered and will be discussed in the corresponding section. The results for each case will be discussed in the following two sections.

#### 5.2.1. Constant Surface Energy

The chemical potential boundary condition,  $\hat{\mu} = 0$ , is applied through ramping of the chemical potential (from  $\mu_0$  to  $\hat{\mu} = 0$ ) over a short time interval  $\Delta t < 10^{-4}$ , to obtain the equilibrium solution under the action of surface stresses. The initial condition for chemical potential,  $\hat{\mu}_0$  is set by prescribing a value for the initial stretch  $\lambda_0$ , Flory's parameter  $\chi$ , and the normalized constant surface free energy per unit current area  $\hat{\gamma}$  as seen in Eq. (6.13). The extent of swelling depends on the initial conditions and material parameters, which can be chosen accordingly depending on the extent of swelling that we want to consider.

Linear poroelasticity theory is effective at predicting experimental results, as long as the experiments are limited to relatively small deformations (Bouklas and Huang, 2012; Yoon et al., 2010). Here we can compare the results of linear theory presented in Section 4, to the finite element simulation to validate the nonlinear theory results (ensuring that we are in the small deformation regime), and also check the limits at which the linear theory gives meaningful results in the presence of elastocapillary phenomena. The material parameters for the simulations corresponding to Fig. 2A and Fig. 3 were chosen to

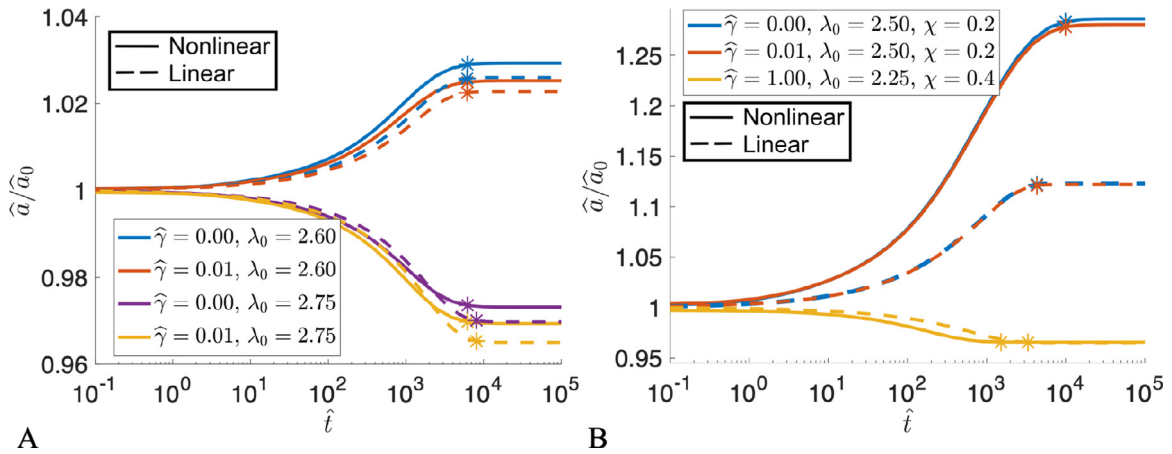


**Fig. 2.** Radial comparisons for the free sphere between nonlinear simulation (solid lines) and linear micro-sphere theory (dashed lines) with and without surface energy. Asterisks indicate the normalized time to 99% equilibrium swelling  $\hat{t}_{eqm}^{99}$ . For all cases, the material parameter  $N\Omega = 10^{-3}$  is constant. A) Small deformation swelling and drying with  $\chi = 0.4$  and B) large deformation swelling and drying with varying  $\chi$ ,  $\lambda_0$ , and  $\tilde{\gamma}$ .

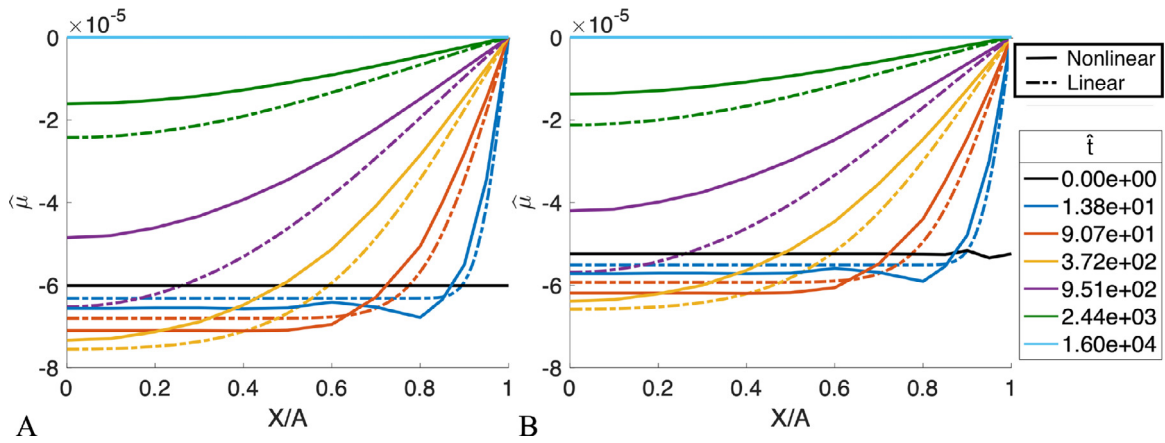


**Fig. 3.** Comparison of chemical potential evolution over normalized time between the nonlinear simulation (solid lines) and the linear microsphere theory (dash dot lines) for normalized surface energy A)  $\tilde{\gamma} = 0.00$  and B)  $\tilde{\gamma} = 0.01$ . The plot is obtained by tracking a set of points along the sphere's radius in the reference configuration. The center of the sphere is at  $X/A = 0$  and point at the outer boundary at  $X/A = 1$ . Material parameters are  $N\Omega = 10^{-3}$  and  $\chi = 0.4$  with an initial stretch of  $\lambda_0 = 2.6$ .

keep the strain from the initial state to equilibrium below 5%. A change to the material parameters indicates whether the system will swell or shrink,  $\tilde{\mu} > \mu_0$  and  $\tilde{\mu} < \mu_0$ , respectively. We are restricting the nonlinear results to the linear regime with this level of strain; therefore, we expect the theories to compare closely.

In Fig. 2 we compare evolution of the normalized radius of the sphere  $\hat{a}$ , over the normalized radius at the initial state  $\hat{a}_0$ , both in the current configuration over time. We consider both swelling and drying responses for both the linear and nonlinear theories, considering the results with and without a surface stresses. The normalized time to 99% of the equilibrium radius,  $\hat{t}_{eqm}^{99}$ , is marked by asterisks in the plots. Overall for both swelling and drying the results between the linear and nonlinear theory agree closely as long as the overall deformation is small, as seen in In Fig. 2A.

We compare the chemical potential profile as a function of the position on a radius of the sphere over time in Fig. 3 again for both theories, considering the results with and without a surface stresses. Examining Fig. 3A, the linear theory is shown to equilibrate more slowly than the nonlinear theory for normalized times  $\hat{t} > 10$ . This result is expected because the linear theory uses a constant mobility tensor while the non-linear theory utilizes a non-constant mobility tensor resulting in an evolving kinetic law governing solvent diffusion (Eq. (2.11)). Fig. 3B shows that a small surface energy value results in faster time to equilibrium. This observation is subtle and is imperceptible in the corresponding radial plots in Fig. 2A. The normalized time to 99% of the equilibrium radius,  $\hat{t}_{eqm}^{99}$ , is marked by asterisks.

In contrast to Fig. 2A, Fig. 2B demonstrates three distinct cases of either large deformations with relatively low elastocapillary effects ( $\tilde{\gamma} = 0.01$ ) or for small deformations with significant elastocapillary effects ( $\tilde{\gamma} = 1$ ). The initial conditions for the large deformation swelling cases, with and without surface energy, were chosen so that overall strain was up to 30%. The drying case in Fig. 2B served to examine the effect of a significant surface energy value under small deformations. To

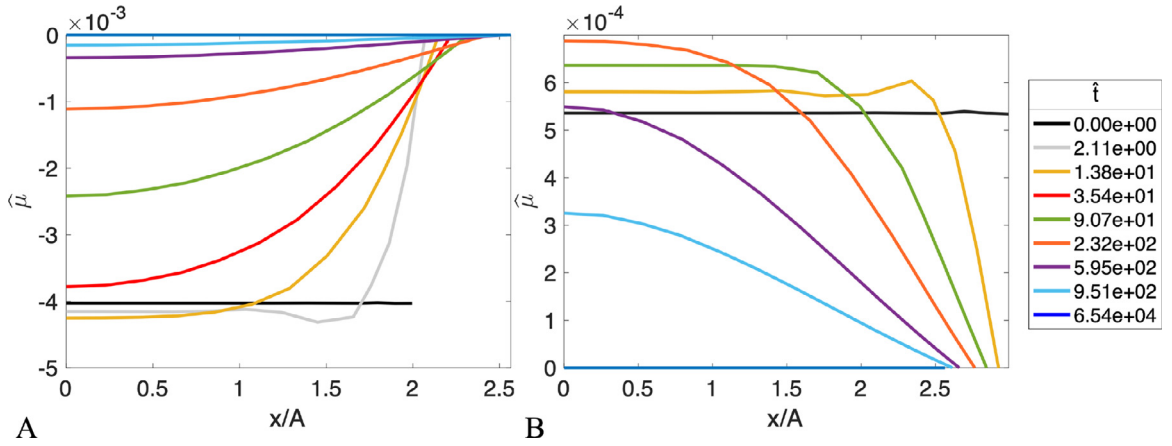


**Fig. 4.** Chemical potential evolution over normalized time from the center to the circumference radial coordinate of the sphere in the current configuration,  $x$ . The center of the sphere is at  $x/A = 0$ . Cases demonstrate significant elastocapillary forces for A) swelling ( $\lambda_0 = 2.0$ ) and B) drying ( $\lambda_0 = 3.0$ ). Other material parameters are  $N\Omega = 10^{-3}$  and  $\chi = 0.2$ .

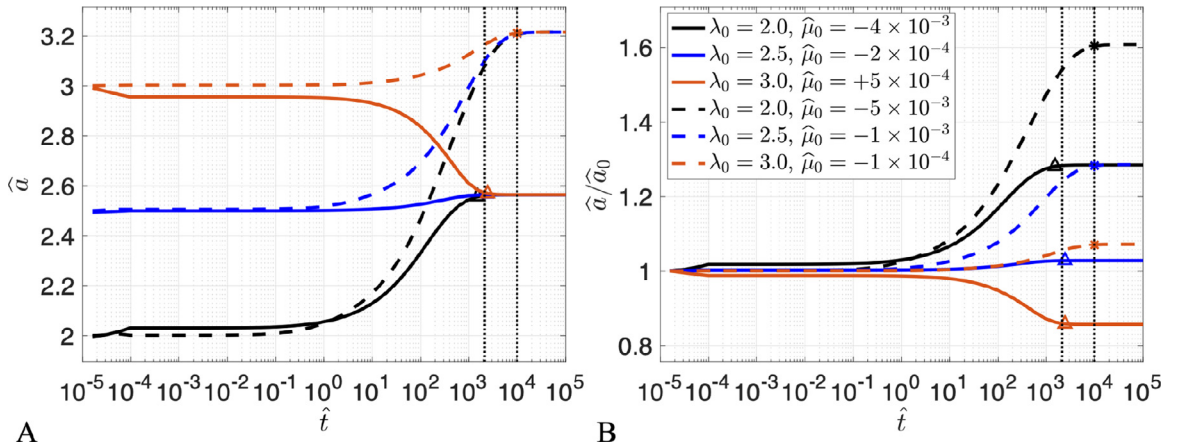


**Fig. 5.** Comparison for the free sphere between cases with a surface energy of  $\hat{\gamma} = 1.0$  (solid lines) and no surface energy (dashed lines). Normalized time versus A) radius and B) radius normalized by the initial radius. Material parameters are  $N\Omega = 10^{-3}$  and  $\chi = 0.2$ . Initial stretches are varied,  $\lambda_0 = 2.0, 2.5, 3.0$ , which produce either a negative or positive initial chemical potential,  $\hat{\mu}_0$ , for swelling or drying cases. The triangles and asterisks indicate the normalized time to 99% equilibrium swelling  $\hat{t}_{eqm}^{99}$ , and the vertical lines are the average of each group respectively.

do this, initial conditions were chosen so that the overall strain was kept at 5%, but a normalized surface energy of  $\hat{\gamma} = 1$  was prescribed. The value of the surface energy,  $\hat{\gamma} = 1$ , leads to an elastocapillary number of  $\hat{n}_{ec} = 1$ , where we expect elastocapillary effects to dominate.

For the large deformation swelling cases, with and without surface energy, we note both the radius increase as well as equilibration time do not match well between the linear and nonlinear results. For the small deformation drying case where  $\hat{\gamma} = 1$ , the final equilibrium radius matches closely, but there is a significant time delay in the linear results. These results demonstrate that the linear theory is sufficient for predictions of hydrogel microsphere transient kinetics under small deformations and for low surface energy values. For large deformations and significant elastocapillary effects, linear theory is not sufficient for predictions of the transient response. This concludes the tests comparing the linear to nonlinear results, and the following results consider only the finite element simulation results.

Here, we examine the nonlinear response with and without a significant normalized surface energy value ( $\hat{\gamma} = 1$ ) at finite deformations. Fig. 4 displays the chemical potential evolution until equilibrium for a swelling and a drying case with a significant surface energy value. We can observe that swelling is not a symmetrical reflection of drying and vice versa (Bertrand et al., 2016). The depth of solvent migration over time into the sphere has implications for the rate at which the hydrogel micro-sphere reaches equilibrium. Fig. 5 demonstrates the transient kinetics of a sphere for different initial stretches,  $\lambda_0$ , with and without a prescribed surface energy (solid vs dashed lines respectively). A key observation is that the equilibration time,  $\hat{t}_{eqm}^{99}$ , is almost an order of magnitude smaller for all drying and swelling cases with surface stresses present (for the specific value of  $\hat{\gamma}$ ); it is interesting that this difference is consistent for microspheres that experience

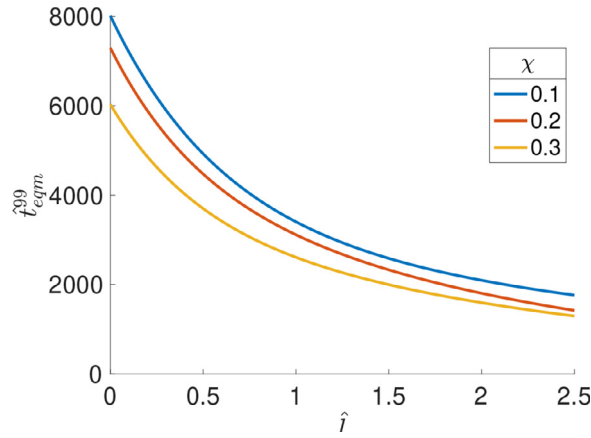


**Fig. 6.** Normalized elastocapillary length scale,  $\hat{l}$ , versus normalized time to 99% radial equilibrium,  $\hat{t}_{eqm}^{99}$ , for  $\chi = 0.1 - 0.3$ . Each line consists of 11 simulations,  $\hat{\gamma} = 0$  to 1 in 0.1 intervals, which were fit by a two-term exponential to obtain a relationship between  $\hat{l}$  and  $\hat{t}_{eqm}^{99}$ .

small (Fig. 5B) as well as large (Fig. 5A) deformation in both drying and swelling. The difference in equilibration time can be attributed to the coupled effects of solvent diffusion, large deformations, and evolving surface stresses.

To obtain some insight towards the time acceleration process in Fig. 5, we consider the spherical hydrogel at the initial state with chemical potential  $\mu_0$  and stretch  $\lambda_0$ . If the chemical potential boundary condition, denoted by  $\tilde{\mu}$ , is larger than the initial chemical potential  $\tilde{\mu} > \mu_0$  then the system will swell, and if  $\tilde{\mu} < \mu_0$  the system will shrink. Focusing on the initial time stages of the swelling case, ( $\hat{t} < 1$ ), solvent only migrates a specific distance  $L(t)$  from the surface into the sphere (See Fig. 4A). Beyond the distance  $H(t)$ , in the unswollen core of the sphere, the chemical potential is constant and can be denoted by  $\mu^*$ . At time  $\hat{t} = 0^+$ , the  $\mu^*$  value is equal to  $\mu_0$ , but the outer layers of the sphere, as they swell, impose a tensile hydrostatic stress on the core of the sphere. This stress state induces a drop in  $\mu^*$ , causing  $\mu^* < \mu_0$ . This phenomena can be observed in the early time steps in Figs. 3 and 4 A. We note a similar procedure for the drying case, Fig. 4B, for which we also observe an increase in equilibration time. Instead of a tensile hydrostatic stress on the core, the outer layers exert a compressive stress which causes an increase in the value of  $\mu^* > \mu_0$ . For swelling cases, the effect of surface stress emerges as the confining hydrostatic stress state that is induced in the unswollen core (as discussed in Appendix B), denoted here as  $\sigma^* < 0$ . This stress value decreases in magnitude as the radius of the sphere increases, because  $\sigma^* \propto 1/a_0$ . The decreased magnitude of  $\sigma^*$  induces a further decrease in  $\mu^*$  solely due to surface effects. The average magnitude of the chemical potential gradient in the radial direction of the swollen spherical layer is  $\nabla_x \mu \cdot \mathbf{A} \approx (\mu^* - \tilde{\mu})/H$ . The flux is dependent on the gradient of the chemical potential (Eq. (2.11)); therefore, the increased chemical potential gradient leads to an increased flux. An increase in the flux of the solvent molecules into the hydrogel microsphere accounts for the accelerated equilibration process under the presence of surface stresses.

We have examined the limiting cases, from no surface energy to a significant value of surface energy. In order to further analyze the effects of elastocapillarity on equilibration time, the initial stretch is fixed at  $\lambda_0 = 2.50$  and the surface energy value  $\hat{\gamma}$  was varied from 0 to 1 in 0.1 intervals for  $\chi = 0.1, 0.2$ , and 0.3. These points were fit with a two-term exponential,  $f(x) = ae^{bx} + ce^{dx}$  where  $x = \hat{t}_{eqm}^{99}$ , for each  $\chi$ . Note that the case of  $\chi = 0.3$  includes both swelling and drying cases, while  $\chi = 0.1$  and 0.2 include only swelling cases. This finding indicates that the time it takes for the microsphere to equilibrate is irrespective of swelling or drying. Fig. 6 demonstrates that an increase in surface energy corresponds to a decrease in equilibration time,  $\hat{t}_{eqm}^{99}$ . With the effect of surface energy, lower  $\chi$  values demonstrate the largest decreases in equilibration time. This prediction is dependent on the material parameters used, but a similar trend is expected for varying the initial stretch values.

In conclusion, Figs. 5 and 6 both illustrate that a non-linear theory taking into account significant elastocapillary effects predicts an accelerated time to equilibration. Specifically, if the surface energy leads to a normalized elastocapillary number of unity, the simulation results equilibrate close to an order of magnitude faster in time compared to the case neglecting surface energy. This finding has strong implications for drug delivery because it indicates a faster drug release rate. Some negative consequences of a faster drug release rate might mean that the drug is released far from the target or has a longer time to be degraded or neutralized by natural processes of the body. Therefore, elastocapillarity must be taken into account during the engineering of micro-sphere drug-delivery systems as it can significantly influence the response of the system.

In recent years there is a significant body of work in surface instabilities of hydrogels (Bouklas et al., 2015b; Dortdivanlioglu and Linder, 2019; Pan et al., 2014; Wu et al., 2013, 2017). In experiments for spherical hydrogels, it has been observed that surface instabilities form and are suppressed transiently during the early swelling process (Bertrand et al., 2016). More specifically, surface creases are expected in the case of a swelling microsphere. For our numerical simulations, the physical instability can lead to divergence as self-contact to prevent interpenetration is not specified in our implementation. Therefore, we consider divergence of the numerical results to indicate the emergence of surface instabilities. It is safe to assume



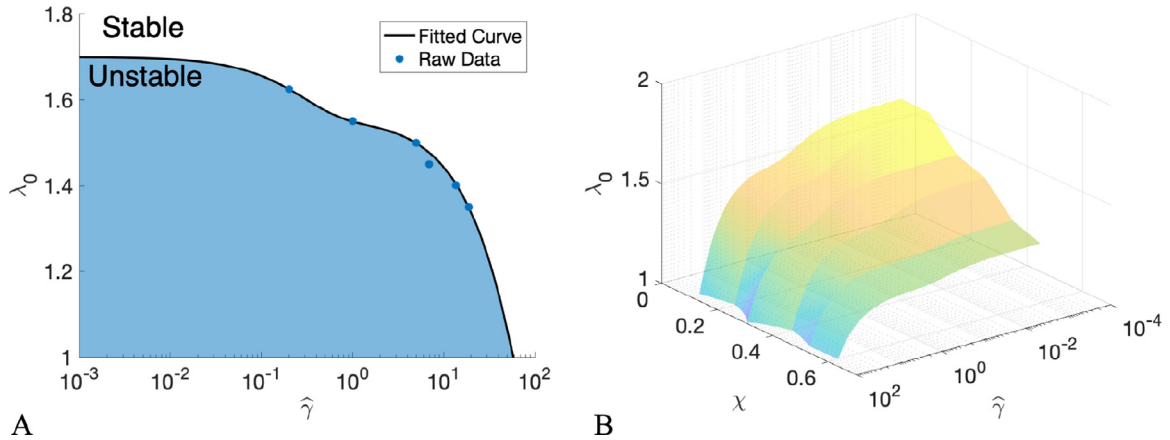


**Fig. 7.** Determining stability based on normalized surface tension, initial stretch, and the Flory parameter. A) Representative example of raw data for  $\chi = 0.1$ , where the raw data is fit with a two-term exponential function ( $f(\hat{\gamma}) = 0.14e^{-3.55\hat{\gamma}} + 1.56e^{-7.61 \times 10^{-3}\hat{\gamma}}$ ) using the nonlinear least squares method (R-square value = 1). B) The same process is repeated from  $\chi = 0.1$  to 0.6 to form an interface between stability and instability, where increasing  $\chi$  shows increasing stability.

that this is the reason that our simulation will diverge for specific cases. Also, we note that creasing is known to be mesh sensitive.

To illustrate the emergence of surface instabilities, we provide an analysis based on three parameters, the normalized (constant) surface energy per unit current area, initial stretch, and the Flory parameter, Fig. 7. Simulations were tested up to 0.1  $\hat{\gamma}$  difference in the interface between stability and instability, and a two-term exponential function ( $f(\hat{\gamma}) = ae^{b\hat{\gamma}} + ce^{d\hat{\gamma}}$ ) was fit to the raw data. Fig. 7A shows the fit for 7 points, where the log x-axis does not display the point that converges at no surface energy contribution,  $\hat{\gamma} = 0$ , ( $\log(0) = -\infty$ ). The same fitting process was carried out from  $\chi = 0.1 - 0.6$ , demonstrating that increased  $\chi$  values display increasing stability (Fig. 7B). This result is expected, because the Flory parameter describes how likely the solvent and the polymer are to mix. Lower  $\chi$  values can yield large swelling stretches, which are more likely to be unstable. Low initial stretch values from 1.1 to 1.5 are unstable, and simulations are more likely to converge for high surface stress. Surface stress, effectively eliminates sharp features at the current configuration, with higher surface energy values it becomes easy to suppress features (like creases) of increasing size. It is clear that the mesh size also dictates the smallest feature sizes in the finite-dimensional solution.

### 5.2.2. Neo-Hookean Surface Energy

Until this point, we have examined the results of a hydrogel microsphere assuming constant surface energy, but we can consider different behaviors for the surface. Gurtin and Murdoch (1975) first raised the question of whether solid surfaces not only hold a residual surface stress but also possess elasticity, surface Lamé constants. A constant surface energy is akin to modeling the surfaces of fluids, the simplest case, which is a reasonable assumption as hydrogels possess a high percentage of water to polymer (Liu et al., 2020c; Style and Xu, 2018). Nevertheless, several experiments have demonstrated that the surface of hydrogels indeed exhibits a more complex material response (Jensen et al., 2017; Xu et al., 2018; 2013). In the context that we are examining, hydrogels immersed in solvent, we expect the surface elasticity to be due to the elastomeric component of the hydrogel instead of the presence of solvent. Interface elasticity instead of surface elasticity would perhaps be a better term, as we are considering a water/hydrogel interface.

We performed simulations to determine how equilibration to a specified level of deformation changes for a Neo-Hookean surface energy compared to a surface with zero (acting as a control) or constant surface energy (per unit current area). The free energy of a Neo-Hookean surface is modeled with the surface Lamé parameters,  $\lambda_b$  and  $\mu_b$ , according to Eq. (2.19). Recall that the initial condition for the chemical potential (Appendix B) only holds for spherical geometries and for a constant surface energy. For the Neo-Hookean surface energy, we use a double ramping scheme instead of simply ramping the chemical potential to zero on the circumference of the sphere. First, the value of the Lamé parameters are ramped from zero to their prescribed value holding the initial chemical potential fixed,  $\tilde{\mu} = \mu_0|_A$ . The shape is allowed to equilibrate holding the boundary condition fixed but letting time evolution progress, then the initial chemical potential is ramped to zero on the outer boundary (over a very short time interval),  $\tilde{\mu} = \mu|_A = 0$  holding the surface free energy fixed. Finally, this structure is allowed to equilibrate to the final state.

To provide an accurate comparison, the initial chemical potential was fixed at  $\hat{\mu}_0 = -2 \times 10^3$  for every simulation. We varied the surface Lamé parameters of the Neo-Hookean surface free energy expression until we achieved a similar deformation to the constant surface energy case (Cases in Fig. 8B  $\lambda_b = \mu_b = 20$  to  $\hat{\gamma} = 1$ ). A Neo-Hookean constitutive surface results in an even faster equilibration time than both the case with no surface energy and the case with a constant surface energy. This result indicates that neglecting surface elasticity of hydrogel microspheres may significantly overestimate equilibration time.



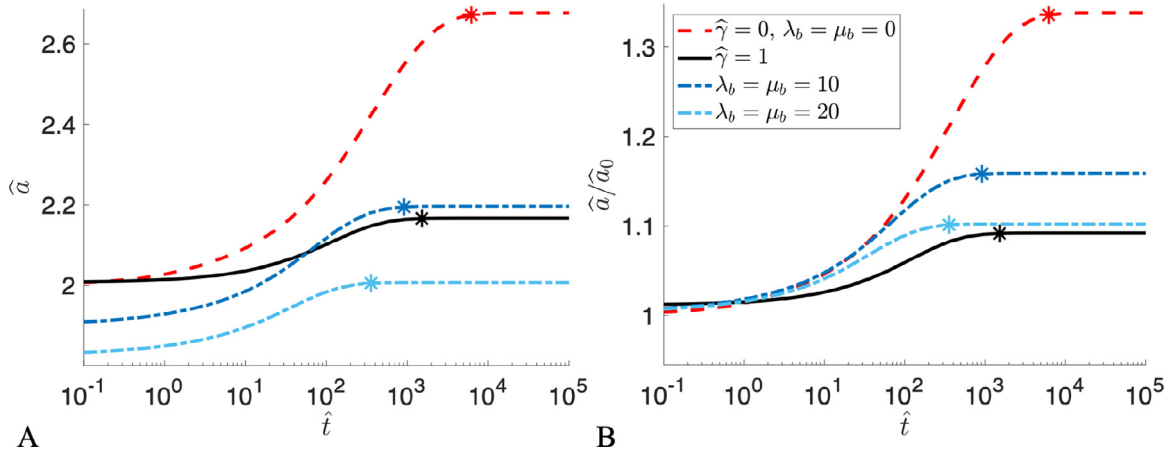


**Fig. 8.** Comparison of constant surface energy (fluid-like boundary potential) versus a Neo-Hookean surface energy to a case with no surface energy. Normalized time versus A) radius and B) radius normalized by the initial radius. Material parameters are  $N\Omega = 10^{-3}$  and  $\chi = 0.4$ , with an initial stretch of  $\lambda_0 = 2.0$ . Initial chemical potential for all cases started from  $\hat{\mu}_0 = -2 \times 10^3$  and was ramped to 0.

### 5.3. Free and Constrained Swelling of a Unit Cube

For nano- and micro-particle fabrication, experimental researchers are not only interested in spherical shapes, but also ellipsoids and parallelepipeds shapes, among other geometries. For example, fabrication methods such as top-down lithography allows for precise control of shape, size, and aspect ratio (Caldorera-Moore et al., 2011). In this method, hydrogel particles are attached to a substrate on one surface and can swell in this configuration during the fabrication process.

Therefore, motivated by these experiments, we consider both free and constrained swelling of a unit cube. For the free swelling case, the cube is constrained to prevent rigid body motions (in the same manner as the free sphere). All surfaces are exposed to an external solvent,  $\hat{\mu} = 0$ , causing swelling to be isotropic. For constrained swelling of a unit cube, the bottom is attached to a substrate so there is no displacement ( $\mathbf{u}|_{x_2=0} = 0$ ) and no flux ( $J_2|_{x_2=0} = 0$ ). The lateral and top surfaces are all exposed to an external solvent,  $\hat{\mu} = 0$ , causing swelling to be anisotropic.

Experimentally, the state in which the hydrogel particle is manufactured/fabricated is considered the initial state. In this initial state, the simulation domain is a cube which is homogeneously swollen, as defined by an initial stretch,  $\lambda_0$ . The cube is discretized uniformly with an equal number of elements along each side,  $n_e = 15$ . The initial chemical potential for the geometries of the free and constrained cube is not known analytically, and the expression in Appendix B. cannot be prescribed on the outer surface. As shown in Fig. 9, we utilize the double ramping scheme explained in Section 5.2.2. The only difference was in the second step (see Fig. 9 step 2), the value of the surface free energy (vs. Lamé constants) is increased while holding a value for the initial chemical potential fixed,  $\hat{\mu} = \mu_0|_A$ . Between steps 2 and 3 in Fig. 9, the structure is allowed to equilibrate, before step 3 which involves ramping of the initial normalized chemical potential ( $\hat{\mu}_0 = -5.0 \times 10^{-3}$ ) to zero.

In Fig. 9, the first case is a classic example of the effects of surface forces, where the model will deform to minimize the surface area with respect to the volume (Javili and Steinmann, 2010). As can be observed, under the application of a significant normalized surface free energy,  $\hat{\gamma} = 1$ , sharp features are minimized and the overall shape becomes spherical. If the surface stress is increased from the value demonstrated, the cube will tend towards a perfect sphere. As shown by Javili and Steinmann (2010), we also expect much more complex shapes under a significant  $\hat{\gamma}$  with no boundary constraints to always achieve a close-to spherical shape.

The second case provides an example of a more complex constrained structure, similar to fabrication states of hydrogel-based nano-scale drug carriers through imprint lithography in Caldorera-Moore et al. (2011). This simulation shows the effect of surface stresses at different stages of the fabrication process on the final particle size and shape. Micro- and nano-particles can exhibit significant size- and shape-dependence, so the numerical predictions must be considered carefully. As follows from the study of the micro-sphere case, the nano-sized particles fabricated through imprint lithography from a flat sheet, exhibit shape changes as well as changes in solvent content based on their size and the intrinsic relationship between surface stress and diffusion.

In our simulation, we demonstrate the effect of constraints on the final equilibrium shape, provided a certain surface energy value and initial chemical potential. It is worth pointing out that upon etching and release from the substrate the nano-particle is expected to attain the same final shape with the free-standing cubic specimen studied previously, but through an alternate transient process, as the initial state is now different. In Caldorera-Moore et al. (2011), several aspect ratios and sizes are studied for the nano-particles. In this work we demonstrate that our theory is capable of obtaining the complex shape changes for these particles, but we do not provide a comprehensive study of aspect ratio, particle size and constraints towards more complex instability phenomena that may take place through the combination of constrained swelling (Bouklas

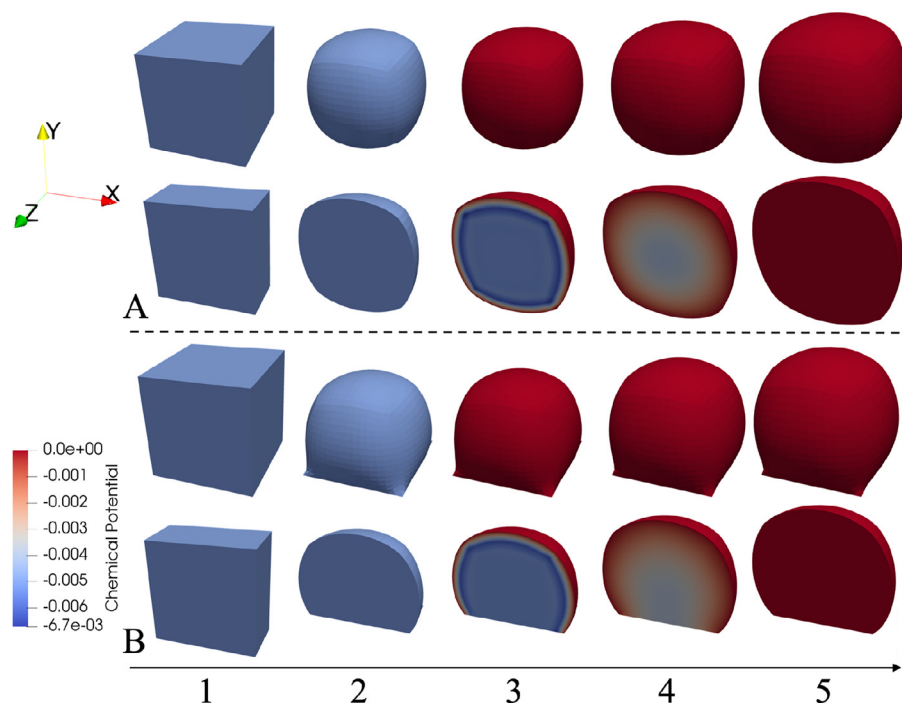


**Fig. 9.** A) Free and B) constrained swelling of a unit cube. In order, the sequence shows 1) initial state set by a homogeneous swelling stretch,  $\lambda_0$ , 2) ramping of normalized surface free energy,  $\hat{\gamma}$  3) ramping of initial normalized chemical potential ( $\hat{\mu}_0 = -5.0 \times 10^{-3}$ ) to zero after initial equilibrium of structure, and 4) progression to equilibrium and 5) final equilibrium state. Material parameters are  $N\Omega = 10^{-3}$  and  $\chi = 0.2$ , with an initial stretch of  $\lambda_0 = 2.0$ .

et al., 2015b; Wu et al., 2013). The latter will be the focus of an upcoming study. It is worth noting that in the presence of extremely large deformation mesh adaptivity might be required.

## 6. Conclusion

A non-linear theory is presented that takes into account mass transport, large deformations, and elastocapillary effects on a hydrogel. A mixed finite element method implemented is implemented in FEniCS. Numerical results are presented for free swelling/drying of a sphere and a cube, as well as constrained swelling of a cube. The non-linear theory is validated by a linear semi-analytical solution for the hydrogel microsphere and the results agree for small deformations with minor surface effects. The key finding is that under introduction of fluid-like surface energy, the hydrogel micro-sphere can equilibrate up to an order of magnitude faster compared to cases without surface energy. Furthermore, a Neo-Hookean surface energy, predicts an even faster equilibration. These results highlight the importance of taking elastocapillary effects into account for biomedical applications such as drug delivery methods. Experimental validation of these findings is extremely important, and to pursue that the authors of this work will further pursue a calibration of the non-linear theory to experimental results across length-scales. In future work, we will focus on the interplay of constraints, large deformation, diffusion and instabilities in the presence of surface stresses. To do so, the introduction of self-contact is required in our implementation, for the study of more complex surface patterns due to folding and creasing.

## Declaration of Competing Interest

The authors declare that they have no known competing financial interests or personal relationships that could have appeared to influence the work reported in this paper.

## CRedit authorship contribution statement

**Ida Ang:** Methodology, Investigation, Software, Visualization, Writing - original draft. **Ze Zhou Liu:** Validation, Formal analysis, Writing - original draft. **Jaemin Kim:** Resources. **Chung-Yuen Hui:** Conceptualization, Supervision, Writing - review & editing. **Nikolaos Bouklas:** Conceptualization, Supervision, Writing - review & editing.

## Acknowledgements

I. Ang acknowledges support from the National Science Foundation Graduate Research Fellowship under Grant No. DGE-1650441. C.Y. Hui acknowledges support by [National Science Foundation](#), USA MoMS program under grant number [1903308](#).

## Appendix A

### Derivation of Eq. 4.9

Compatibility implies that

$$\varepsilon_r = (r\varepsilon_\theta)_{,r} \Leftrightarrow \frac{\varepsilon_r - \varepsilon_\theta}{r} = \frac{\partial \varepsilon_\theta}{\partial r} \Leftrightarrow \frac{(\sigma_r - \sigma_\theta)}{r} = 2G_0 \frac{\partial \varepsilon_\theta}{\partial r} \quad (6.1)$$

In the last step, we have used  $(\sigma_r - \sigma_\theta) = 2G_0(\varepsilon_r - \varepsilon_\theta)$  which is obtained by subtracting (4.3) b by (4.3) a. The last equation in Eq. (6.1), using the equilibrium Eq. (4.13) can be rewritten as:

$$\frac{(\sigma_r - \sigma_\theta)}{r} = -\frac{1}{2} \frac{\partial \sigma_r}{\partial r} = 2G_0 \frac{\partial \varepsilon_\theta}{\partial r} \Rightarrow \varepsilon_\theta = -\frac{\sigma_r}{4G} + f(t) \quad (6.2)$$

which is Eq. (4.9)

### Derivation of Eq. 4.13

First, eliminate  $\varepsilon_r$  in Eq. (4.10) using compatibility, this result in

$$\frac{1}{2G} \sigma_r - \frac{\partial (r\varepsilon_\theta)}{\partial r} - \frac{(6K_0 - 4G_0)}{(4G_0 + 3K_0)} f(t) - \frac{3}{4G_0 + 3K_0} p = 0 \quad (6.3)$$

Next, we substitute Eq. (4.9) into Eq. (6.3), we obtain the following linear first order differential equation governing the radial stress,

$$3\sigma_r + r \frac{\partial \sigma_r}{\partial r} = \frac{36K_0G_0}{(4G_0 + 3K_0)} f(t) + \frac{12G_0}{(4G_0 + 3K_0)} p \quad (6.4)$$

The bounded solution of Eq. (6.4) is Eq. (4.13).

### Derivation of Eq. 4.21

Let  $\phi = P - P^*$ , then Eq. (4.17) can be rewritten as:

$$\frac{\partial \phi}{\partial \hat{T}} - \frac{1}{R} \frac{\partial^2 (R\phi)}{\partial R^2} = 4 \frac{df}{d\hat{T}}, \quad R < 1, \hat{T} > 0 \quad (6.5)$$

The initial and boundary conditions are changed to:

$$\phi(R, \hat{T} = 0^-) = -P_0, \quad \phi(R = 1, \hat{T} > 0) = 0 \quad (6.6)$$

We look for a series solution of the form:

$$\phi = \sum_{n=1}^{\infty} \frac{\sin(n\pi R)}{R} H_n(\hat{T}) \quad (6.7)$$

Substituting Eq. (6.6) into Eq. (6.5) results in

$$\sum_{n=1}^{\infty} \left( \frac{dH_n(\hat{T})}{d\hat{T}} + n^2 \pi^2 H_n(\hat{T}) \right) \sin(n\pi R) = 4R \frac{df}{d\hat{T}} \quad (6.8)$$

Expand the right hand side of Eq. (6.8) into a Fourier sine series, i.e.,

$$4R \frac{df}{d\hat{T}} = \frac{8}{\pi} \frac{df}{d\hat{T}} \sum_{n=1}^{\infty} \frac{(-1)^{n+1}}{n} \sin(n\pi R) \quad (6.9)$$

Equating both sides of Eq. (6.8) and 6.9 and using the orthogonality of the sine functions, we obtain

$$\left( \frac{dH_n(\hat{T})}{d\hat{T}} + n^2 \pi^2 H_n(\hat{T}) \right) = \frac{8}{\pi} \frac{df}{d\hat{T}} \frac{(-1)^{n+1}}{n} \quad (6.10)$$

The solution of Eq. (6.10) satisfying the initial condition Eq. (6.6) is Eq. (4.21).

## Appendix B

Following Green and Zerna (1992) and Steinmann (2008), we introduce the total curvature denoted by  $c = -\bar{\nabla}_x \cdot \mathbf{n}$  where  $\mathbf{n}$  is the unit normal vector on the surface, which is twice the mean curvature,  $\bar{\kappa}$ ,  $c = 2\bar{\kappa}$ .

At the initial state, the hydrogel sphere is under a non-zero hydrostatic stress state, resulting from the surface stresses that effectively induces a constant normal traction on the free surface of the sphere. Under these conditions, the Cauchy principal stress specialized in the radial direction is  $\sigma_r = -c\gamma = -2\gamma\bar{\kappa}$ , where  $\bar{\kappa}$  is the mean curvature of a sphere given in the *current configuration*. The mean curvature is  $\bar{\kappa} = 1/a_0 = 1/(\lambda_0 A)$  when specializing to the initial swelling state of the sphere, with current radius  $a_0$  yielding,

$$\sigma_r = -2\gamma\bar{\kappa} = -\frac{2\gamma}{\lambda_0 A} \quad (6.11)$$

The constitutive expression for the radial component of the Cauchy stress given in spherical coordinates for the state of deformation at the initial state following Bertrand et al. (2016), is

$$\sigma_r = \frac{\lambda_0}{J} \frac{\partial}{\partial \lambda_0} U_e + \frac{d}{df} U_m - \frac{\mu_0}{\Omega} \quad (6.12)$$

Substituting Eq. (6.11) and the free energy of elastic stretching and mixing, Eq. (2.12) and 2.13, into the constitutive relationship, Eq. (6.12), and solving for the initial chemical potential, we can obtain the following normalized expression

$$\hat{\mu}_0 = N\Omega \left( \frac{1}{\lambda_0} - \frac{1}{\lambda_0^3} \right) + \frac{1}{\lambda_0^3} + \log \left( 1 - \frac{1}{\lambda_0^3} \right) + \frac{\chi}{\lambda_0^6} + N\Omega \frac{2\hat{\gamma}}{\lambda_0}. \quad (6.13)$$

Given this expression, one can calculate the initial swelling stretch  $\lambda_0$  given the initial chemical potential  $\mu_0$  or vice-versa. This simplifies the double ramping scheme which is necessary for general shapes and surface free energy models (see Section 5.3 for more detail).

## References

- Agarwal, R., Singh, V., Journey, P., Shi, L., Sreenivasan, S.V., Roy, K., 2013. Mammalian cells preferentially internalize hydrogel nanodiscs over nanorods and use shape-specific uptake mechanisms. *Proc. Natl. Acad. Sci.* 110 (43), 17247–17252. doi:[10.1073/pnas.1305000110](https://doi.org/10.1073/pnas.1305000110).
- Ahn, S.-K., Kasi, R.M., Kim, S.-C., Sharma, N., Zhou, Y., 2008. Stimuli-responsive polymer gels. *Soft Matter* 4, 1151–1157. doi:[10.1039/B714376A](https://doi.org/10.1039/B714376A).
- Alawiye, H., Kuhl, E., Goriely, A., 2019. Revisiting the wrinkling of elastic bilayers i: linear analysis. *Philos. Trans. R. Soc. A* 377 (2144), 20180076.
- Alnæs, M.S., Blechta, J., Hake, J., Johansson, A., Kehlet, B., Logg, A., Richardson, C., Ring, J., Rognes, M.E., Wells, G.N., 2015. The fenics project version 1.5. *Arch. Numer. Softw.* 3 (100). doi:[10.11588/ans.2015.100.20553](https://doi.org/10.11588/ans.2015.100.20553).
- Bertrand, T., Peixinho, J., Mukhopadhyay, S., MacMinn, C.W., 2016. Dynamics of swelling and drying in a spherical gel. *Phys. Rev. Appl.* 6, 064010. doi:[10.1103/PhysRevApplied.6.064010](https://doi.org/10.1103/PhysRevApplied.6.064010).
- Bhattarai, N., Gunn, J., Zhang, M., 2010. Chitosan-based hydrogels for controlled, localized drug delivery". *Adv. Drug Deliv. Rev.* 62 (1), 83–99. doi:[10.1016/j.addr.2009.07.019](https://doi.org/10.1016/j.addr.2009.07.019).
- Bico, J., Reyssat, Roman, B., 2018. Elastocapillarity: when surface tension deforms elastic solids. *Annu. Rev. Fluid Mech.* 50 (1), 629–659. doi:[10.1146/annurev-fluid-122316-050130](https://doi.org/10.1146/annurev-fluid-122316-050130).
- Biot, M.A., 1941. General theory of three dimensional consolidation. *J. Appl. Phys.* 12 (2), 155–164. doi:[10.1063/1.1712886](https://doi.org/10.1063/1.1712886).
- Bouklas, N., Huang, R., 2012. Swelling kinetics of polymer gels: comparison of linear and nonlinear theories. *Soft Matter* 8, 8194–8203. doi:[10.1039/C2SM25467K](https://doi.org/10.1039/C2SM25467K).
- Bouklas, N., Landis, C.M., Huang, R., 2015. Effect of solvent diffusion on crack-tip fields and driving force for fracture of hydrogels. *J. Appl. Mech.* 82 (8), 1–16. doi:[10.1115/1.4030587](https://doi.org/10.1115/1.4030587).
- Bouklas, N., Landis, C.M., Huang, R., 2015. A nonlinear, transient finite element method for coupled solvent diffusion and large deformation of hydrogels. *J. Mech. Phys. Solids* 79, 21–43. doi:[10.1016/j.jmps.2015.03.004](https://doi.org/10.1016/j.jmps.2015.03.004).
- Caldorera-Moore, M., Kang, M.K., Moore, Z., Singh, V., Sreenivasan, S.V., Shi, L., Huang, R., Roy, K., 2011. Swelling behavior of nanoscale, shape- and size-specific, hydrogel particles fabricated using imprint lithography. *Soft Matter* 7, 2879–2887. doi:[10.1039/C0SM01185A](https://doi.org/10.1039/C0SM01185A).
- do Carmo, M.P., 1976. *Differential geometry of curves and surfaces*. Prentice Hall.
- Chen, S., Huang, R., Ravi-Chandar, K., 2020. Linear and nonlinear poroelastic analysis of swelling and drying behavior of gelatin-based hydrogels", *Journal of International Journal of Solids and Structures* 195, 43–56. doi:[10.1016/j.jisols.2020.03.017](https://doi.org/10.1016/j.jisols.2020.03.017).
- Chester, S.A., 2012. A constitutive model for coupled fluid permeation and large viscoelastic deformation in polymeric gels. *Soft Matter* 8, 8223–8233. doi:[10.1039/C2SM25372K](https://doi.org/10.1039/C2SM25372K).
- Chester, S.A., Leo, C.V.D., Anand, L., 2015. A finite element implementation of a coupled diffusion-deformation theory for elastomeric gels. *Int. J. Solid. Struct.* 52, 1–18. doi:[10.1016/j.jisols.2014.08.015](https://doi.org/10.1016/j.jisols.2014.08.015).
- Choi, N.W., Cabodi, M., Held, B., Gleghorn, J.P., Bonassar, L.J., Stroock, A.D., 2007. Microfluidic scaffolds for tissue engineering. *Nat. Mater.* 6 (11), 908–915. doi:[10.1038/nmat2022](https://doi.org/10.1038/nmat2022).
- Delavoipière, J., Tran, Y., Verneuil, E., Heurtefeu, B., Hui, C.Y., Chateauminois, A., 2018. Friction of poroelastic contacts with thin hydrogel films. *Langmuir* 34 (33), 9617–9626.
- Dortdivanlioglu, B., Linder, C., 2019. Diffusion-driven swelling-induced instabilities of hydrogels. *J. Mech. Phys. Solids* 125, 38–52. doi:[10.1016/j.jmps.2018.12.010](https://doi.org/10.1016/j.jmps.2018.12.010).
- Duda, F.P., Souza, A.C., Fried, E., 2010. A theory for species migration in a finitely strained solid with application to polymer network swelling. *J. Mech. Phys. Solids* 58 (4), 515–529. doi:[10.1016/j.jmps.2010.01.009](https://doi.org/10.1016/j.jmps.2010.01.009).
- Elkhoury, K., Russell, C.S., Sanchez-Gonzalez, L., Mostafavi, A., Williams, T.J., Kahn, C., Peppas, N.A., Arab-Tehrany, E., Tamayol, A., 2019. Soft-nanoparticle functionalization of natural hydrogels for tissue engineering applications. *Adv. Healthc. Mater.* 8 (18), 1900506. doi:[10.1002/adhm.201900506](https://doi.org/10.1002/adhm.201900506).
- Fernandes, R., Gracias, D., 2012. Self-folding polymeric containers for encapsulation and delivery of drugs. *Adv. Drug Deliv. Rev.* 64, 1579–1589. doi:[10.1016/j.addr.2012.02.012](https://doi.org/10.1016/j.addr.2012.02.012).
- Flory, P.J., 1953. *Principles of Polymer Chemistry*. Cornell University Press, Ithaca, NY.
- Flory, P.J., Rehner, J., 1943. Statistical mechanics of cross linked polymer networks ii. swelling. *J. Chem. Phys.* 11 (11), 521–526. doi:[10.1063/1.1723792](https://doi.org/10.1063/1.1723792).
- Geuzaine, C., Remacle, J.-F., 2009. Gmsh: a 3-d finite element mesh generator with built-in pre- and post-processing facilities. *Int. J. Numer. Methods Eng.* 79 (11), 1309–1331. doi:[10.1002/nme.2579](https://doi.org/10.1002/nme.2579).

- Green, A.E., Zerna, W., 1992. Theoretical Elasticity. Courier Corporation.
- Gurtin, M.E., Murdoch, A.I., 1975. A continuum theory of elastic material surfaces. *Arch. Ration. Mech. Anal.* 57 (4), 291–323.
- Gurtin, M.E., Murdoch, I.A., 1978. Surface stress in solids. *Int. J. Solids Struct.* 14 (6), 431–440. doi:10.1016/0020-7683(78)90008-2.
- Henann, D.L., Bertoldi, K., 2014. Modeling of elasto-capillary phenomena. *Soft Matter* 10, 709–717. doi:10.1039/C3SM52583J.
- Hennink, W., van Nostrum, C., 2002. Novel crosslinking methods to design hydrogels. *Adv. Drug Deliv. Rev.* 54 (1), 13–36. doi:10.1016/S0169-409X(01)00240-X.
- Holzappel, G.A., 2000. *Nonlinear solid mechanics II*. John Wiley & Sons, Inc..
- Hong, W., Zhao, X., Zhou, J., Suo, Z., 2008. A theory of coupled diffusion and large deformation in polymeric gels. *J. Mech. Phys. Solids* 56 (5), 1779–1793. doi:10.1016/j.jmps.2007.11.010.
- Huggins, M.L., 1941. Solutions of long chain compounds. *J. Chem. Phys.* 9 (5), 440.
- Hui, C.Y., Jagota, A., Lin, Y.Y., Kramer, E.J., 2002. Constraints on microcontact printing imposed by stamp deformation. *Langmuir* 18, 1394–1407. doi:10.1021/la0113567.
- Hui, C.-Y., Lin, Y.Y., Chuang, F.-C., Shull, K.R., Lin, W.-C., 2006. A contact mechanics method for characterizing the elastic properties and permeability of gels. *J. Polym. Sci., Part B: Polym. Phys.* 44 (2), 359–370. doi:10.1002/polb.20613.
- Hui, C.-Y., Liu, T., Salez, T., Raphael, E., Jagota, A., 2015. Indentation of a rigid sphere into an elastic substrate with surface tension and adhesion. *Proc. Math. Phys. Eng. Sci.* 471. doi:10.1098/rspa.2014.0727.
- Javili, A., McBride, A., Steinmann, P., Reddy, B.D., 2014. A unified computational framework for bulk and surface elasticity theory: a curvilinear-coordinate-based finite element methodology. *Comput. Mech.* 54, 745–762. doi:10.1007/s00466-014-1030-4.
- Javili, A., Steinmann, P., 2009. A finite element framework for continua with boundary energies. part i: the two-dimensional case. *Comput. Methods Appl. Mech. Eng.* 198 (27), 2198–2208. doi:10.1016/j.cma.2009.02.008.
- Javili, A., Steinmann, P., 2010. A finite element framework for continua with boundary energies. part ii: the three-dimensional case. *Comput. Methods Appl. Mech. Eng.* 199 (9), 755–765. doi:10.1016/j.cma.2009.11.003.
- Jensen, K.E., Style, R.W., Xu, Q., Dufresne, E.R., 2017. Strain-dependent solid surface stress and the stiffness of soft contacts. *Phys. Rev. X* 7, 041031. doi:10.1103/PhysRevX.7.041031.
- Kang, M.K., Huang, R., 2010. Effect of surface tension on swell-induced surface instability of substrate-confined hydrogel layers. *Soft Matter* 6, 5736–5742. doi:10.1039/C0SM00335B.
- Krischok, A., Linder, C., 2019. A generalized inf-sup test for multi-field mixed-variational methods. *Comput. Methods Appl. Mech. Eng.* 357, 112497. doi:10.1016/j.cma.2019.06.008.
- Lapinski, N., Liu, Z., Yang, S., Hui, C.-Y., Jagota, A., 2019. A surface with stress, extensional elasticity, and bending stiffness. *Soft Matter* 15, 3817–3827. doi:10.1039/C9SM00075E.
- Li, T., Suo, Z., 2006. Deformability of thin metal films on elastomer substrates. *Int. J. Solids Struct.* 43 (7), 2351–2363. doi:10.1016/j.ijsolstr.2005.04.034.
- Liu, Z., Bouklas, N., Hui, C.-Y., 2020. Coupled flow and deformation fields due to a line load on a poroelastic half space: effect of surface stress and surface bending. *Proc. R. Soc. A* 476 (2233), 20190761. doi:10.1098/rspa.2019.0761.
- Liu, Z., Jagota, A., Hui, C.-Y., 2020. Modeling of surface mechanical behaviors of soft elastic solids: theory and examples. *Soft Matter* 16, 6875–6889. doi:10.1039/D0SM00556H.
- Liu, Z., Jensen, K., Xu, Q., 2020. Effects of strain-dependent surface stress on the adhesive contact of a rigid sphere to a compliant substrate. *Soft Matter* 15, 2223–2231. doi:10.1039/c8sm02579g.
- Liu, Z., Toh, W., Ng, T.Y., 2015. Advances in mechanics of soft materials: a review of large deformation behavior of hydrogels. *Int. J. Appl. Mech.* 07 (05), 1530001. doi:10.1142/S1758825115300011.
- Logg, A., Mardal, K.-A., Wells, G.N., et al., 2012. Automated Solution of Differential Equations by the Finite Element Method. Springer doi:10.1007/978-3-642-23099-8.
- Lucantonio, A., Nardinocchi, P., Teresi, L., 2013. Transient analysis of swelling-induced large deformations in polymer gels. *J. Mech. Phys. Solids* 61 (1), 205–218.
- Mailand, E., Li, B., Eyckmans, J., Bouklas, N., Sakar, M.S., 2019. Surface and bulk stresses drive morphological changes in fibrous microtissues. *Biophys. J.* 117 (5), 975–986. doi:10.1016/j.bpj.2019.07.041.
- McBride, A., Javili, A., Steinmann, P., Bargmann, S., 2011. Geometrically nonlinear continuum thermomechanics with surface energies coupled to diffusion. *J. Mech. Phys. Solids* 59 (10), 2116–2133. doi:10.1016/j.jmps.2011.06.002.
- McNamee, J., Gibson, R.E., 1960. Displacement functions and linear transforms applied to diffusion through porous elastic media. *Q. J. Mech. Appl. Math.* 13 (1), 98–111. doi:10.1093/qjmam/13.1.98.
- Mora, S., Maurini, C., Phou, T., Fromental, J., Audoly, B., Pomeau, Y., 2013. Solid drops: large capillary deformations of immersed elastic rods. *Phys. Rev. Lett.* 111. doi:10.1103/PhysRevLett.111.114301.
- Okumura, D., Kawabata, H., Chester, S.A., 2020. A general expression for linearized properties of swollen elastomers undergoing large deformations. *J. Mech. Phys. Solids* 135, 103805. doi:10.1016/j.jmps.2019.103805.
- Pan, K., Ni, Y., He, L., Huang, R., 2014. Nonlinear analysis of compressed elastic thin films on elastic substrates: from wrinkling to buckle-delamination. *Int. J. Solids Struct.* 51 (21), 3715–3726. doi:10.1016/j.ijsolstr.2014.07.005.
- Peppas, N., Hilt, J., Khademhosseini, A., Langer, R., 2006. Hydrogels in biology and medicine: from molecular principles to bionanotechnology. *Adv. Mater.* 18 (11), 1345–1360. doi:10.1002/adma.200501612.

- Polygerinos, P., Correll, N., Morin, S.A., Mosadegh, B., Onal, C.D., Petersen, K., Cianchetti, M., Tolley, M.T., Shepherd, R.F., 2017. Soft robotics: review of fluid-driven intrinsically soft devices; manufacturing, sensing, control, and applications in human-robot interaction. *Adv. Eng. Mater.* 19 (12), 1700016. doi:[10.1002/adem.201700016](https://doi.org/10.1002/adem.201700016).
- Rice, J.R., Cleary, M.P., 1976. Some basic stress diffusion solutions for fluid-saturated elastic porous media with compressible constituents. *Rev. Geophys.* 14 (2), 227–241. doi:[10.1029/RG014i002p00227](https://doi.org/10.1029/RG014i002p00227).
- Scherer, G.W., 1989. Drying gels: Viii. revision and review. *J. Non Cryst. Solids* 109 (2), 171–182. doi:[10.1016/0022-3093\(89\)90029-X](https://doi.org/10.1016/0022-3093(89)90029-X).
- Steichen, S.D., Calderera-Moore, M., Peppas, N.A., 2013. A review of current nanoparticle and targeting moieties for the delivery of cancer therapeutics. *Eur. J. Pharmaceutical Sci.* 48 (3), 416–427. doi:[10.1016/j.ejps.2012.12.006](https://doi.org/10.1016/j.ejps.2012.12.006).
- Steigmann, D.J., Ogden, R.W., 1999. Elastic surface-substrate interactions. *Proc. R. Soc. Lond. A* 455, 437–474.
- Steinmann, P., 2008. On boundary potential energies in deformational and configurational mechanics. *J. Mech. Phys. Solids* 56 (3), 772–800. doi:[10.1016/j.jmps.2007.07.001](https://doi.org/10.1016/j.jmps.2007.07.001).
- Style, R.W., Jagota, A., Hui, C.-Y., Dufresne, E.R., 2017. Elastocapillarity: surface tension and the mechanics of soft solids. *Annu. Rev. Condens. Matter Phys.* 8 (1), 99–118. doi:[10.1146/annurev-conmatphys-031016-025326](https://doi.org/10.1146/annurev-conmatphys-031016-025326).
- Style, R.W., Xu, Q., 2018. The mechanical equilibrium of soft solids with surface elasticity. *Soft Matter* 14, 4569–4576. doi:[10.1039/C8SM00166A](https://doi.org/10.1039/C8SM00166A).
- Sun, W., Ostien, J.T., Salinger, A.G., 2013. A stabilized assumed deformation gradient finite element formulation for strongly coupled poromechanical simulations at finite strain. *Int. J. Numer. Anal. Methods Geomech.* 37 (16), 2755–2788. doi:[10.1002/nag.2161](https://doi.org/10.1002/nag.2161).
- Wu, Z., Bouklas, N., Huang, R., 2013. Swell-induced surface instability of hydrogel layers with material properties varying in thickness direction. *Int. J. Solids Struct.* 50 (3), 578–587. doi:[10.1016/j.ijsolstr.2012.10.022](https://doi.org/10.1016/j.ijsolstr.2012.10.022).
- Wu, Z., Bouklas, N., Liu, Y., Huang, R., 2017. Onset of swell-induced surface instability of hydrogel layers with depth-wise graded material properties. *Mech. Mater.* 105, 138–147. doi:[10.1016/j.mechmat.2016.11.005](https://doi.org/10.1016/j.mechmat.2016.11.005).
- Xu, Q., Style, R.W., Dufresne, E.R., 2018. Surface elastic constants of a soft solid. *Soft Matter* 14, 916–920. doi:[10.1039/C7SM02431B](https://doi.org/10.1039/C7SM02431B).
- Xu, X., Jagota, A., Peng, S., Luo, D., Wu, M., Hui, C.-Y., 2013. Gravity and surface tension effects on the shape change of soft materials. *Langmuir* 29 (27), 8665–8674. doi:[10.1021/la400921h](https://doi.org/10.1021/la400921h).
- Yoon, J., Cai, S., Suo, Z., Hayward, R.C., 2010. Poroelastic swelling kinetics of thin hydrogel layers: comparison of theory and experiment. *Soft Matter* 6, 6004–6012. doi:[10.1039/C0SM00434K](https://doi.org/10.1039/C0SM00434K).
- Zhang, Y., Tekobo, S., Tu, Y., Zhou, Q., Jin, X., Dergunov, S.A., Pinkhassik, E., Yan, B., 2012. Permission to enter cell by shape: nanodisk vs nanosphere. *ACS Appl. Mater. Interfaces* 4 (8), 4099–4105. doi:[10.1021/am300840p](https://doi.org/10.1021/am300840p).